

國立臺灣大學電機資訊學院光電工程學研究所

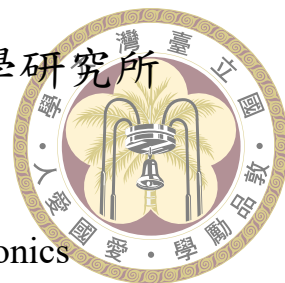
博士論文

Graduate Institute of Photonics and Optoelectronics

College of Electrical Engineering and Computer Science

National Taiwan University

Doctoral Dissertation



基於矽光平台上之 O-band 1×4 分波(解)多工濾波器

O-band 1×4 wavelength division (de)multiplexing filters
based on Silicon Photonics

鍾國方

Kuo-Fang Chung

指導教授：黃定洧 博士

Advisor: Ding-Wei Huang Ph.D.

中華民國 111 年 9 月

September, 2022

國立臺灣大學博士學位論文

口試委員會審定書



基於矽光平台上之 O-band 1×4 分波 (解) 多工
濾波器

O-band 1×4 wavelength division (de)multiplexing
filters based on Silicon Photonics

本論文係鍾國方君（學號 D08941008）在國立臺灣大學
光電工程學研究所完成之博士學位論文，於民國 111 年 9 月
26 日承下列考試委員審查通過及口試及格，特此證明

口試委員：

黃定湧

(指導教授)

林晃嚴

章彌彥

張祐嘉

邱華恭

所長

吳育任



致謝

從台大入學到能夠完成博士學位，真的要非常感謝父母無怨無悔地付出。還記得三年前決定要攻讀博士學位時，從家裡的不支持到後來的諒解，無不再提醒自己必須全力以赴盡快畢業。也非常感謝黃定洧教授對學生的栽培，讓我在相對自由的研究環境下對自己的未來負責，並且培養出不畏懼新事物、自主學習的良好習慣。再來要感謝台灣科技部及台大提供的椰林獎學金，讓我也能夠在不接受家裡金援或在外兼職的狀況下完全專注在研究上，完成三年來的諸多計畫與研究。

最後，期望本篇論文的內容能夠帶給讀者更多靈感、對矽光子領域有所貢獻。



摘要

分波(解)多工元件由於大數據、雲端運算、及物聯網的蓬勃發展而被廣泛地使用在商業與學術用途。由於製程誤差與環境溫度的影響，分波(解)多工器與光源的雷射波長會偏移而與預期的通道波長不同。為了解決這個現象，本篇論文提出兩個研究包含電控熱調式陣列波導光柵以及布拉格光柵反向耦合器以解決之。

本論文提出一個利用 S 型陣列波導光柵中兩個三角區域補償相位的特點來設計光譜雙向可調的分波多工濾波器。在額外增加電控熱調機制於此兩區域後，元件可以在其中一個區域外加電壓之後得到光譜紅(藍)移以匹配所需的分波系統通道波長。為了降低所需電壓及模擬維度，電控熱調的電極及加熱區走線我們使用串聯至特定單位數目後再並聯的方式達成。此外，鑑於大折射率對比所帶來的小元件佔地面積、導波層較大的熱光係數、以及鎢材的高熱導率，我們可以預見位移矽基元件之濾波響應所需的熱能相比其他平台小。從實際製作出的元件我們量測得到 ± 30.5 奈米/瓦的線性且雙向可調的調製效率，即使只使用正的熱光係數材質，若外加電壓範圍 0 至 2.5 伏特其可調製範圍約 8 奈米。相比其他目前已紀錄之熱調式陣列波導光柵，此研究的雙向可調特性、高調製效率、超低需求電壓、以及大的可調範圍完勝它們，顯示此元件對於分波(解)多工系統的潛力。

另一方面，本論文亦提出一個利用布拉格光柵反向耦合器，以達到平頭式(平頂)、超低串擾的濾波響應符合大通道間距分波系統所需。為了放寬布拉格週期



所需的最小線寬，我們使用有較小折射率之氮化矽而非矽作為導波層來實現此元件。此外，為了將通道串擾降得更低以及更有效率地設計出期望的共振波長，我們利用基於微擾式介電常數的耦合模態理論得出恰當的多模波導布拉格光柵兩側之寬度瓦楞。模擬結果顯示元件達到超低通道串擾 -25.5 分貝、超低額外損耗小於 0.3 分貝、超大的製程容忍度 ± 18 奈米、以及超寬 -25 分貝之串擾可用帶寬約 13.5 奈米。透過 S 參數觀念將四個波導布拉格光柵與刪除信號元件串接，我們得到有著(甲)超低額外損耗 < 0.6 分貝、(乙)高通道均勻度 > -0.45 分貝、(丙)寬的 1 分貝帶寬約 13.45 奈米、以及(丁)超低的 < -28 分貝之串擾可用帶寬約 14.35 奈米的平頂濾波響應效能。製程誤差分析顯示在極端的 ± 18 奈米之製程誤差下，通道串擾仍然維持在 < -25 分貝而不影響到額外損耗或帶寬。相較其他目前已知的大通道間距分波(解)多工系統濾波器，本研究提出的元件擁有超低損耗的平頂濾波響應、接近陣列波導光柵的超低通道串擾、以及最寬的 -28 分貝之串擾可用帶寬，顯示此元件對於大通道間距分波多工電信傳輸系統的強大潛力與魅力。

關鍵字：矽光子、可調制式陣列波導光柵、波導布拉格光柵、多模波導、分波(解)多工器



Abstract

Thanks to the well development of big data, cloud computing, and the Internet of Things, wavelength division (de)multiplexing (WDM) systems have been widely utilized in commercial and academic use. Due to fabrication errors and increased environmental temperature, the spectral peak wavelengths of WDM filters and the lasing wavelengths of optical sources would deviate from the desired channels wavelengths. To address this, two studies are proposed and presented in this dissertation, including thermally tunable arrayed waveguide grating (AWG) and Bragg grating-assisted contra-directional coupler (BGACDC).

In Chapter 3, two triangular region with complementary phase distributions in an S-shaped AWG are leveraged and chosen as the thermal-tuning regions controlled by electrical voltages. Red (Blue) shifted spectra can be achieved by applying voltages on one of two regions, to meet the desired channel wavelengths. In order to reduce the required electrical voltages and the dimension degree used in simulation model, a parallel configuration



and a concept of heater unit are respectively employed for the circuit. In addition, three aspects including (i) larger thermo-optic coefficient, (ii) smaller device footprint brought by high-index contrast, and (iii) higher thermal conductivity of the tungsten allow for the lower requirement of the thermal power to shift the filtering responses, compared to other platform. From the simulation results, a linear and bi-directional tuning efficiency approximately ± 30.5 nm/W, in spite of using only materials with positive thermo-optic coefficients, is achieved at a tuning range of 8 nm in the electrical voltage range of 0–2.5 V. Given the bi-directional tunable feasibility, the ultra-high tuning efficiency, the ultra-low required voltages, and the wide tuning range, the device demonstrated in this study outperforms other thermally tunable AWGs proposed in the known literature, showing its great potential for the WDM systems.

On the other hand, a BGACDC is proposed to achieve flap-top filtering responses with ultra-low crosstalk (XT) for coarse WDM (CWDM) systems. To relax the critical dimension required for the Bragg period in O-band, silicon nitride with lower index instead of silicon is used to realize the device. In order to further reduce the channel XT and evaluate the desired resonant wavelength more efficiently, an appropriate width corrugations for both side walls of the multi-mode waveguide Bragg grating are utilized based on the perturbed-permittivity coupled mode theory. The simulation results show that ultra-low



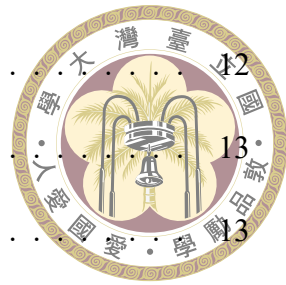
channel XTs < -25.5 dB, ultra-low excess losses (ELs) < 0.3 dB, an ultra-high fabrication tolerance of ± 18 nm, and ultra-broad available bandwidths of 13.5 nm for channel XTs below -25 dB (ABW_{25-dB}) are achieved. To evaluate performances of the overall filter formed by four cascaded BGACDCs and identical broadband signal dropping devices, the overall CWDM filter offers flat-top responses with ultra-low ELs < 0.6 dB, a high channel uniformity > -0.45 dB, broad 1-dB bandwidths ~13.45 nm, ultra-low XTs < -28 dB, and ultra-broad ABWs_{28-dB} ~14.35 nm. Analysis of the tolerance showed that XTs of the overall filter remained < -25 dB even for extreme cases with ± 18 -nm over-etching errors without compromising the ELs or BWs. Compared to other CWDMs proposed in the literature to date, the device proposed in this study has the ultra-low EL with flat-top responses, ultra-low XT which is competitive with the AWGs, and the broadest ABW_{28-dB}, illustrating its great potential and high attractiveness for use in the CWDM telecommunication systems.

Keywords: Silicon Photonics, tunable arrayed waveguide grating, waveguide Bragg grating, multi-mode waveguide, wavelength division (de)multiplexer



Contents

	Page
Verification Letter from the Oral Examination Committee	i
致謝	ii
摘要	iii
Abstract	v
Contents	viii
List of Figures	xi
List of Tables	xiv
Chapter 1 Introduction	1
1.1 Wavelength division (de)multiplexing (WDM) filters	1
1.1.1 Arrayed waveguide grating (AWG)	3
1.1.2 Bragg grating-assisted WDM filter	5
1.2 Dissertation configuration	6
Chapter 2 Theoretical Background	8
2.1 Working principle of AWG	8
2.2 Working principle of thermal tuning	10
2.3 Working principle of Bragg grating-assisted WDM filters	10
2.3.1 Coupled-mode theory for permittivity perturbation	10



2.3.2 Transfer matrix method	12
2.4 Simulation methods	13
2.4.1 Beam propagation method (BPM)	13
2.4.2 Heat Transport (HT) solver	14
2.4.3 Finite-difference eigenmode (FDE) solver	15
2.4.4 Finite-difference time-domain (FDTD) solver	16
Chapter 3 Thermally bi-directionally tunable (TBDT) AWG	20
3.1 Simulation for passive design	21
3.2 Simulation for active design	25
3.3 Measurement results	27
3.4 Discussion	32
3.5 Summary	35
Chapter 4 Bragg grating-assisted WDM filter	36
4.1 Device structure and optimization	37
4.2 Analysis of fabrication tolerance	46
4.3 Summary	49
Chapter 5 Conclusion	51
5.1 Summary	51
5.2 Suggestion for future work	53
References	54
Appendix A — Phase correction for RSoft simulation model	69
A.1 Phase correction	69



Appendix B — Adaptive particle swarm algorithm (APSO)

B.1	Introduction	72
-----	------------------------	----

Appendix C — Automated python process flow for Lumerical optimization on

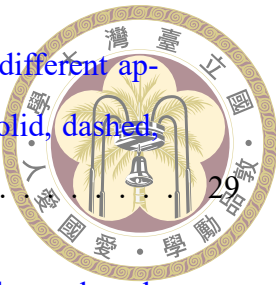
Taiwania 3 handled by local PC	72
--------------------------------	----

C.1	Introduction	72
-----	------------------------	----



List of Figures

1.1	Schematic configuration of a conventional AWG.	3
1.2	Microscope images of an AWG for 1×8 WDM system	4
1.3	SEM images of the AWG shown in Fig. 1.2	4
1.4	Schematic configuration of a WBG.	5
1.5	SEM images of the fabricated gratings with various misalignment lengths.	6
1.6	(a) Schematic layout and (b) SEM images of a WBG for filtering out TE mode.	6
2.1	(a) Schematic function of demultiplexing for WDM system. (b) Enlarged schematic view of the second slab region	8
2.2	Yee's Cell for solving time- and space-dependent electric and magnetic fields.	19
3.1	Schematic configuration of the proposed S-shaped TBDTAWG.	21
3.2	Simulated field distributions of the output star coupler operated at four channel wavelengths.	24
3.3	Simulated filtering responses of the proposed AWG for the O-band CWDM configuration.	25
3.4	Simulated refractive index difference (left y axis) of each heater unit and the corresponding wavelength shifts (right y axis) of filtering response in terms of different (a) thermal powers and (b) applied electrical voltages. .	27
3.5	(a) Mask layout of the proposed TBDTAWG and (b) photograph of the fabricated device on the SOI chip.	28



3.6 (a) Red-shifted and (b) blue-shifted filtering responses for different applied voltages V_B of 0, 1, 2, and 2.5 V are represented by solid, dashed, dotted, and dash-dotted lines, respectively.	29
3.7 Effective index differences (left y axis) of adjacent AWs and wavelength shifts (right y axis) of filtering response in terms of electrical voltages at four output Channels 1.27, 1.29, 1.31, and 1.33 μm for (a–d) red-shift tuning and (e–h) blue-shift tuning, where the solid line and squared red marker represent the simulated results from Fig. 3.4 and the measured data from Fig. 3.6, respectively.	30
3.8 The linear relationship between the spectrum shifts and the required thermal powers at four output Channels 1.27, 1.29, 1.31, and 1.33 μm for (a–d) red-shift tuning and (e–h) blue-shift tuning, where the solid line and squared red marker represent the simulated results from Fig. 3.4 and the measured data from Fig. 3.6, respectively.	31
3.9 Scheme for automatically stabilizing the spectral responses of thermally bi-directionally tunable AWG for WDM communication systems. CWLPLD, continuous-wave low-power laser diode; SAWG, S-shaped arrayed waveguide grating; PD, photodiode; DA, electrical differential amplifier; D, diode; RSH, red-shifting heater; BSH, blue-shifting heater; TBDTAWG, thermally bi-directionally tunable arrayed waveguide grating. Green and blue routing wires represent optical and electrical connections, respectively.	32
4.1 Schematic (a) 3-D and (b) top views of the proposed MMWBG.	37
4.2 Effective refractive indices of the first three TE modes versus core widths for four channel wavelengths.	40
4.3 Simulated filtering responses using 3-D FDTD method for $\lambda_{\text{ch}} = 1.27 \mu\text{m}$ in terms of $\Lambda_{\text{ch}} = 392 \text{ nm}$ and different maximum width corrugations Δw .	41



4.4	Simulated filtering responses of (a) the contra-directional coupled TE ₁ mode, (b) the remaining forward TE ₀ mode, and (c)–(f) the electric-field top-view profiles at the given four channel wavelengths, respectively, for the corresponding individual MMWBGs using the 3-D FDTD solutions in terms of the parameter set (W , Δw , s) = (950 nm, 65 nm, 5).	43
4.5	Schematic top view of the SiN _x -based BADC for broadband coupling from the TE ₁ mode at through port to the TE ₀ mode at cross port.	44
4.6	(a) Simulated transmission (blue) of the TE ₀ mode at cross port, and extinction ratio (red) between the dropped TE ₀ and remaining TE ₁ modes. (b)–(g) Electric-field profiles at six wavelengths.	45
4.7	(a) Schematic configuration of the proposed overall O-band CWDM filter and (b) its simulated filtering responses.	46
4.8	Simulated filtering responses of the individual MMWBGs using 3-D FDTD method at the four channels in terms of the configuration in Fig. 4.1 and the given over-etching errors W_e within (± 18 nm) with a step of 6 nm.	48
4.9	Simulated filtering responses of the overall CWDM filter using 3-D FDTD method followed by cascaded S-parameter calculation at the four channels in terms of the configuration in Fig. 4.7 and the given over-etching errors W_e	49
B.1	Adaptive parameters for APSO.	71



List of Tables

3.1	Thermal-tuning performance comparison of thermally tunable AWGs in the literature.	31
4.1	Required Bragg periods for the four-channel CWDM system.	40
4.2	Optimal parameter set of SiN _x -based BADC.	44
4.3	Performance comparison of CWDM filters in the literature.	47

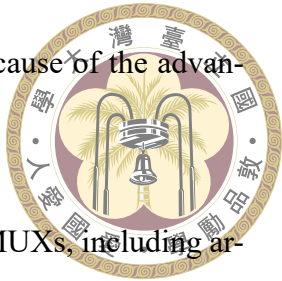


Chapter 1 Introduction

1.1 Wavelength division (de)multiplexing (WDM) filters

Owing to the rapid developments of big data, cloud computing, and the Internet of Things, demands for telecommunication systems with higher transmission rates and larger data capacities are increasing annually. To meet the requirements, wavelength division (de)multiplexing (WDM) system has been reported and widely used for commercial and scientific purposes. [1, 2]. In WDM systems, multiple optical signals operated at different channel wavelengths as well as different spatial locations are multiplexed into one physical fiber/waveguide or vice versa by using (de)multiplexing filters, namely multiplexers/demultiplexers (MUXs/DEMUXs), so that the used number of fibers between the transceiver chips can be decreased, leading to larger data capacities for telecommunication systems. To date, many MUXs/DEMUXs based on different mechanisms and platforms [2–10, 10–61] have been implemented for desired filtering responses to improve the system. Among these platforms, silicon-on-insulator (SOI) is one of the most promising candidates for photonics integrated circuits (PICs) given the compatibility with complementary metal-oxide-semiconductor (CMOS) lithographic technology and the high maturity as well as low cost for fabrication and mass production. In recent years, Silicon Photonics (SiPh) based on SOI platform has become more and more popular for PICs

[7, 8, 15, 19–23, 26, 28, 29, 32, 35, 37–41, 43, 52, 53, 55, 57, 61–85] because of the advantages.



There are many mechanisms used to realize on-chip MUXs/DEMUXs, including arrayed waveguide grating (AWG) [2–25, 46, 47], echelle grating (EG) [26, 37–39], angled multi-mode interferometer (AMMI) [34–36], Mach–Zehnder interferometer-based (MZI-based) lattice filter [52–60], Bragg grating-assisted contra-directional coupler (BGACDC) [30–32, 40–45]. Arrayed waveguide grating and echelle grating are widely utilized in commercial and academic use, owing to its ultra-low crosstalk (XT). However, these two are based on the spatial diffraction, leading to an inevitable insertion loss (IL) of 3–5 dB due to the diffraction loss to other unused orders. Despite this native restriction, the devices are commonly used for both dense-WDM (DWDM) and coarse-WDM (CWDM) systems given their long-term development. For the second mechanism, *i.e.*, AMMI, the self-imaging behavior of MMI is wavelength- and spatial-dependent, and consequently the WDM can be realized if angled ports are arranged, however, at the expense of extremely long length of the device [34–36]. In addition, either angled ports or angled MMI employed in the device should be avoided given the grid discretization of patterns might lead to unwanted performance degradation. In general, first three mechanisms usually bring about non-flat-top filtering responses and IL above 1–1.5 dB. On the other hand, ultra-low ILs at peak wavelengths of channels with flat-top responses can be achieved with MZI-based lattice filter or BGACDC. Although low crosstalk can be obtained in MZI-based lattice filter using broadband power splitter such as bent directional coupler (BDC), the BDC with a fixed bending gap is still a complex pattern to be implemented.

In this dissertation, two MUXs/DEMUXs based on different mechanisms [10, 19–25, 30–32, 40–51] over the SOI platform are studied and briefly introduced in the following

subsections.



1.1.1 Arrayed waveguide grating (AWG)

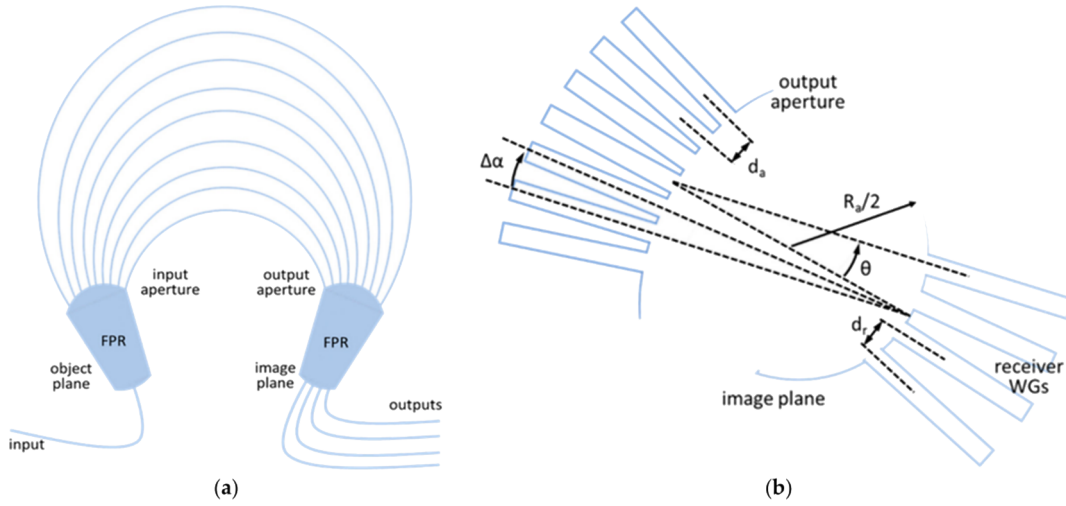


Figure 1.1: Schematic configuration of a conventional AWG [86].

One of the most commonly used mechanisms for (de)multiplexing optical signals is arrayed waveguide grating (AWG) [2, 87, 88] given the ultra-low crosstalk leveraging large number of arrayed waveguides and low-index contrast between core and cladding brought by platform such as silica and silicon nitride. Schematic configuration of a conventional AWG is given in Fig. 1.1 [86] for 1×4 WDM system. Figures 1.2 and 1.3 show microscope images and SEM images of a silicon-nitride AWG presented in [86] for 1×8 wavelength (de)multiplexing. From the figures, an AWG is composed of two star couplers with each one formed by a free-propagation region (FPR) and optical ports in connection with phase-controlling arrayed waveguides and with other devices. By using both imaging and dispersive properties brought by FPRs and arrayed waveguides (AWs), respectively, AWG can be designed so that the optical beam is focused at the desired spatial ports in terms of corresponding spectral channel wavelengths for (de)multiplexing and thus increasing the data capacity [2]. In general cases, spectral peak wavelengths of

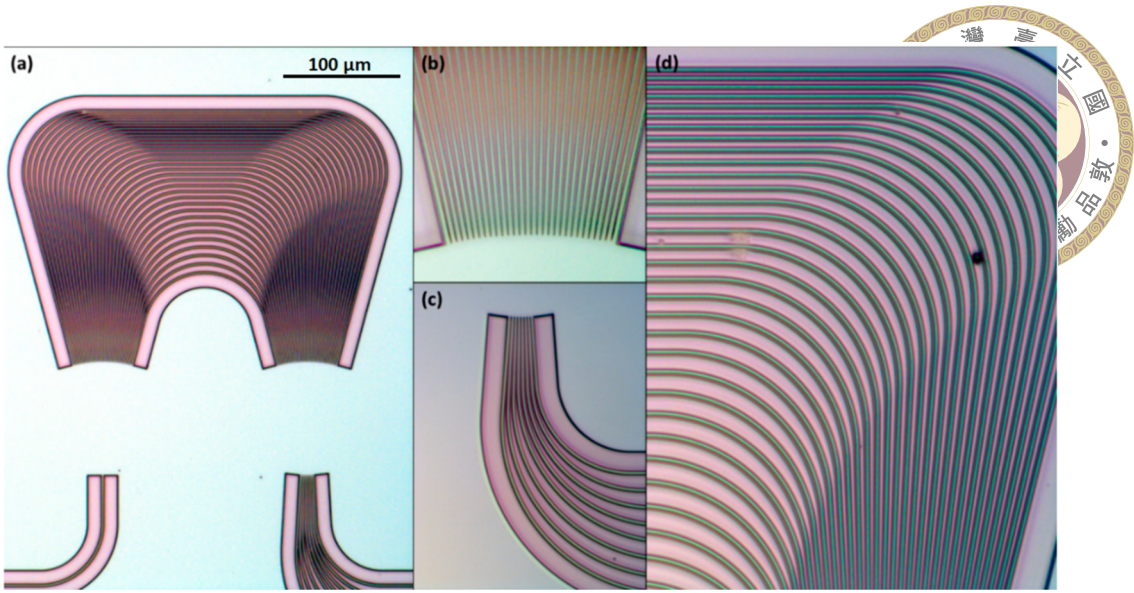


Figure 1.2: Microscope images of an AWG for 1×8 WDM system [86].

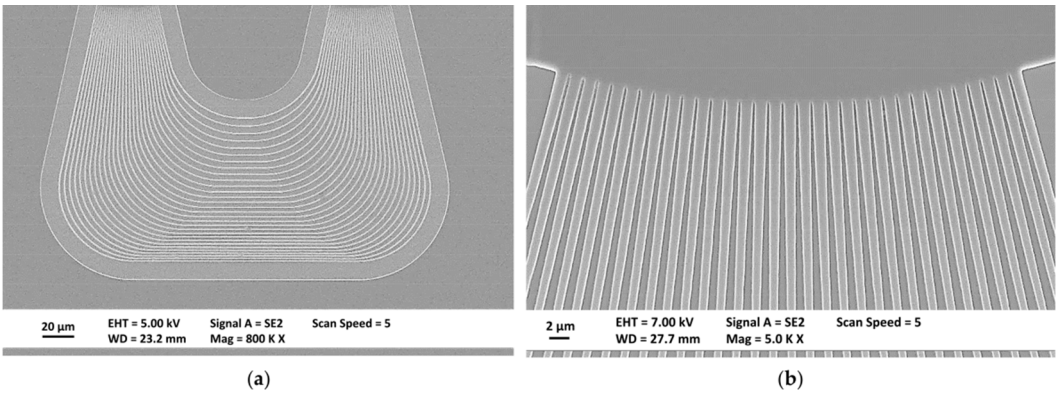
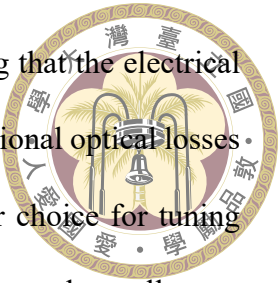


Figure 1.3: SEM images of the AWG shown in Fig. 1.2 [86].

Gaussian-like filtering profiles of AWGs and lasing wavelengths of optical sources might be deviated from the desired channel wavelengths due to fabrication errors and increased environmental temperature, respectively, degrading the performances of interest of the telecommunication system. To address the issue, two methods including flattening the top of spectral responses [2, 4–18] and shifting the overall spectrum [83, 84, 89–92] to the desired spectral peak wavelengths have been utilized. Although a flat spectral response can be realized with approaches such as a double image [2, 4–13] or sinc-like field profile [14–18], excess losses (ELs) of all channels are normally increased by 2–5 dB, which is a critical issue for transceiver modules used in telecommunication realm. For the second method, shifted spectra can be obtained with refractive index changes using



either thermal or electrical tunings on silicon-based chip. Considering that the electrical one involves refractive index changes in imaginary part inducing additional optical losses and that the tuning speed is not required, the thermal one is a better choice for tuning without compromising the insertion loss of AWGs. In this dissertation, a thermally tunable AWG (TTAWG) is proposed and implemented with the foundry service provided by Interuniversity Microelectronics Centre (IMEC), to achieve aligned spectral responses for better performance. Details for the simulation and the measurement will be presented and demonstrated, respectively, in Chapter 3

1.1.2 Bragg grating-assisted WDM filter

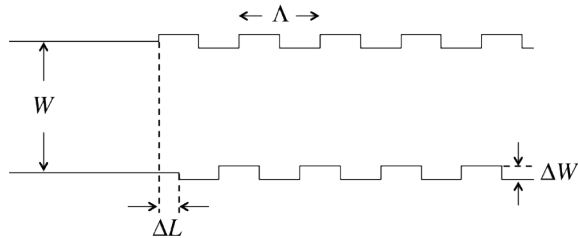


Figure 1.4: Schematic configuration of a WBG [78].

Another method to relax the misalignments among peak wavelengths of filtering response brought by (de)multiplexer, lasing wavelengths of optical sources, and desired channel wavelengths is using coarse-WDM (CWDM) instead of dense-WDM (DWDM) systems. To achieve this while remaining a low EL, a different mechanism based on Bragg grating structure (BGS) [30–32, 78, 79, 93–95] is employed for CWDM configuration [40–45]. In the literature [40–45], flat-top responses with ultra-low ELs and ultra-high channels uniformity can be obtained with designed waveguide Bragg gratings (WBGs). To improve the CWDM system, an efficient design methodology of the WBG with ultra-low crosstalks (XTs), broad available bandwidth under ultra-low XT, and high fabrication tolerance is proposed in this dissertation.

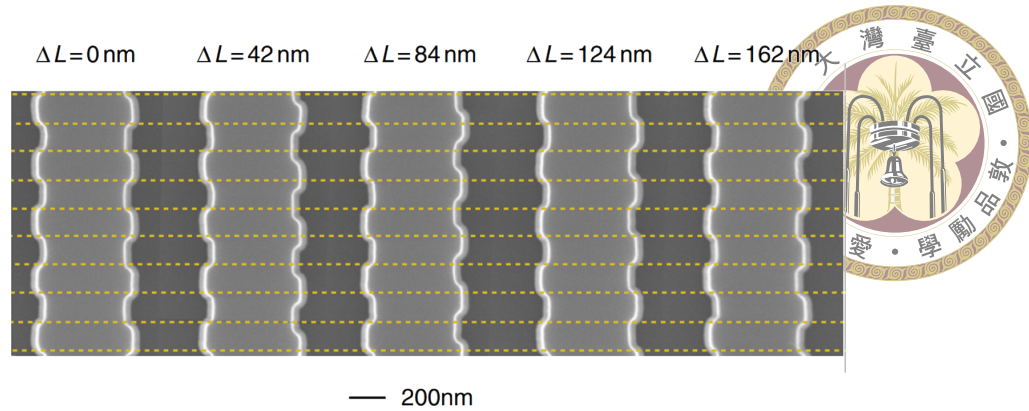


Figure 1.5: SEM images of the fabricated gratings with various misalignment lengths [78].

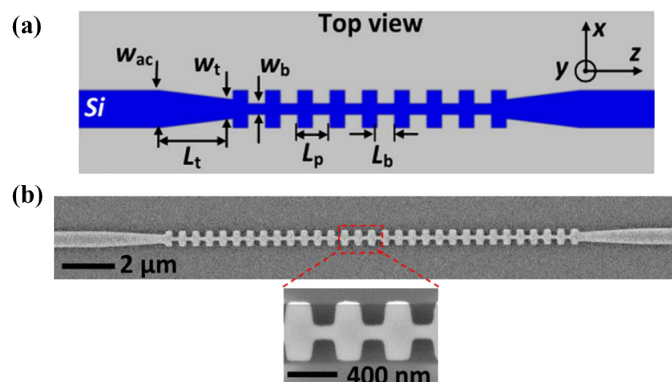


Figure 1.6: (a) Schematic layout and (b) SEM images of a WBG for filtering out TE mode [79].

1.2 Dissertation configuration

This dissertation starts with the introduction in Chapter 1, illustrating research motivation and objectives. In Chapter 2, basic theories for the researches are given, including working principle of AWG (Section 2.1), thermal tuning (Section 2.2), and WBG (Section 2.3). For efficient design and analysis of the devices, four solutions including beam propagation method (BPM) (Section 2.4.1), heat transport method (Section 2.4.2), finite difference eigenmode (FDE) method (Section 2.4.3), and finite-difference time-domain (FDTD) method (Section 2.4.4) provided by commercial softwares are utilized in the studies, and briefly introduced in the corresponding subsections.

In Chapter 3, a thermally bi-directional tuning feasibility is proposed and demonstrated on an S-shaped AWG at ultra-low voltage using parallel-circuit configuration.

In Chapter 4, a design methodology of WBG is presented to obtain ultra-low XTs and high fabrication tolerance. Moreover, an engineered amplitude apodization based on permittivity-perturbed coupled-mode theory (PPCMT) is employed for accurate evaluation of the resonant wavelength brought by maximum contra-directional coupling coefficient, decreasing the difficulty of designing such devices and the side-lobe imbalance (SLI). At the end of this dissertation, summary and suggestions for future work are given in Chapter 5.





Chapter 2 Theoretical Background

2.1 Working principle of AWG

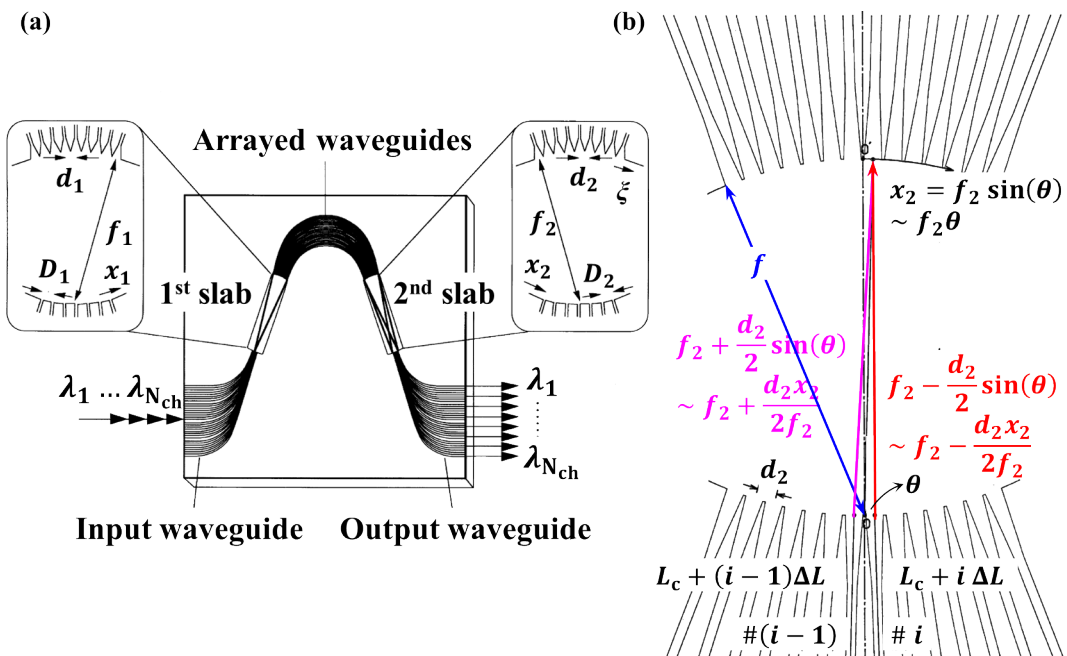
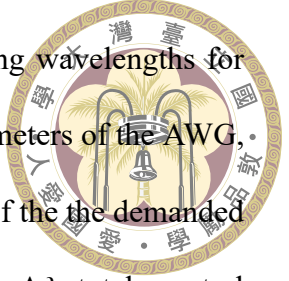


Figure 2.1: (a) Schematic function of demultiplexing [88] for WDM system. (b) Enlarged schematic view of the second slab region [88].

The working principle of AWG is presented in [87, 88], with the schematic configuration shown in Fig. 2.1. The device is formed by two free-propagation regions (FPRs) with phased-arrayed waveguides as a connection between them. The lengths of phased-arrayed waveguides are designed to obtain the specific dispersive property. By leveraging the dispersive property featured by incremental length difference of arrayed waveguides denoted in the figure, the optical beams in the second slab can be engineered and fo-



cused at the desired output waveguide ports in terms of corrsponding wavelengths for (de)multiplexing. To efficiently evaluate the required geometric parameters of the AWG, the following equations (2.1)–(2.7) are utilized step by step in terms of the the demanded WDM parameters, including central wavelength λ_0 , channel spacing $\Delta\lambda$, total spectral channel numbers N_{ch} , ports pitch $D = D_1$ as well as $d = d_1$, fundamental-mode effective index of arrayed (slab) waveguides $n_{\text{eff}_0}(n_s)$, and the critical dimension d_c .

$$\Delta\lambda_{\text{FSR}} = N_{\text{ch}}\Delta\lambda, \quad (2.1)$$

$$m' = \frac{\lambda_0}{\Delta\lambda_{\text{FSR}}}, \quad (2.2)$$

$$m = \text{round} \left(m' \frac{n_{\text{eff}_0}}{N_g} \right), \quad (2.3)$$

$$N_g = n_{\text{eff}_0} - \lambda \frac{dn_{\text{eff}_0}}{d\lambda}, \quad (2.4)$$

$$\Delta L_0 = m \frac{\lambda_0}{n_{\text{eff}_0}}, \quad (2.5)$$

$$f = R_o = 2 R_i = \frac{n_s d D}{m' \Delta\lambda}, \quad (2.6)$$

$$D_{\text{FSR}} = D N_{\text{ch}}, \quad (2.7)$$

where ΔL_0 , m , N_g , f , $\Delta\lambda_{\text{FSR}}$ and D_{FSR} represent the length difference between adjacent arrayed waveguides, diffraction order, fundamental-mode group index of arrayed waveguides, radius of curvature, wavelength free spectral range, and free spatial range of ports arrangement. R_i and R_o denote the radii of curvature of image planes at the interfaces between input/output ports and the FPRs.



2.2 Working principle of thermal tuning

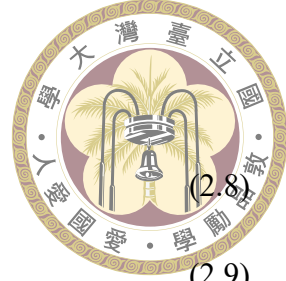
To date, some thermally tunable AWG leveraging the relation between heat and material refractive indices are implemented on different platforms [83, 84, 89–92]. Normally, a thermo-optic coefficient of $1.68 \cdot 10^{-4} /K$ is utilized for silicon layer. For more accurate evaluation, two-dimensional (2-D) simulations are performed using the heat transportation followed by the finite-difference eigenmode (FDE) solver to obtain the thermal-diffusion as well as the refractive index change profiles at different electrical voltages.

2.3 Working principle of Bragg grating-assisted WDM filters

Recently, a mechanism based on Bragg grating-assisted contra-directional coupling have been used to achieve a flat-top filtering response for CWDM system. To demonstrate the working principle of the device, two concepts including perturbed-permittivity coupled-mode theory (PPCMT) and its analytical expression for brief evaluation of resulting spectrum are given in the following two subsections.

2.3.1 Coupled-mode theory for permittivity perturbation

The differential equations for Bragg grating-assisted contra-directional coupling are minimally adjusted based on the perturbed-permittivity coupled-mode theory for fiber



Bragg grating presented in [1], and given in the following

$$\frac{\partial B_\mu}{\partial z} = j\kappa_{dc,\mu\mu}B_\mu + j\kappa_{ac,v\mu}A_v \cdot e^{-j(\Delta\beta z - \phi(z))},$$

$$\frac{\partial A_v}{\partial z} = -j\kappa_{dc,vv}A_v - j\kappa_{ac,\mu v}B_\mu \cdot e^{j(\Delta\beta z - \phi(z))}, \quad (2.9)$$

$$\kappa_{dc,(vv,\mu\mu)} = \frac{\omega\epsilon_0}{4} \iint \Delta\epsilon_{r,dc}(x, y) \mathbf{E}_{v,\mu}(x, y) \cdot \mathbf{E}_{v,\mu}^*(x, y) dx dy, \quad (2.10)$$

$$\kappa_{ac,(v\mu,\mu v)} = \frac{\omega\epsilon_0}{4} \iint \Delta\epsilon_{r,ac}(x, y) \mathbf{E}_{v,\mu}(x, y) \cdot \mathbf{E}_{\mu,v}^*(x, y) dx dy, \quad (2.11)$$

where z is the spatial position along the propagation direction. A and B represent the transverse guided-mode amplitudes, and v and μ denote the desired forward and backward propagation modes, respectively. The parameters ω , ϵ_0 , and $\epsilon_{r,(dc,ac)}$ represent the optical operating angular frequency, the free-space permittivity, and the perturbation profiles of the relative dielectric constant, respectively. The wavelength-dependent parameters κ , $\Delta\beta$, and ϕ are the coupling coefficient, phase mismatch (detuning), and spatially varying phase change, respectively. The coupling coefficients κ_{dc} and κ_{ac} are obtained by the overlap integration in terms of dc and ac terms of the permittivity perturbation profile, respectively, and the modes during coupling, whereas \mathbf{E} denotes the normalized transverse electric fields of the guided modes, as given in (2.10) and (2.11). In (2.8) and (2.9), each differentiated amplitude is dominated by two aspects including dc and ac terms. The dc term is attributed to the variation of the propagation constant of the guided mode, while the ac term results from the coupling between two guided modes, owing to permittivity perturbation by the grating structure.



2.3.2 Transfer matrix method

To describe the contra-directional coupling behavior more clearly with mathematical expression, a transfer matrix in terms of eigenvalue α_{ei} is derived as

$$\begin{bmatrix} R(z) \\ S(z) \end{bmatrix} = \begin{bmatrix} T_{11}(z) & T_{12}(z) \\ T_{21}(z) & T_{22}(z) \end{bmatrix} \begin{bmatrix} R(0) \\ S(0) \end{bmatrix}, \quad (2.12)$$

$$T_{11(22)}(z) = \cosh(\alpha z) \bar{j} \frac{\delta}{\alpha} \sinh(\alpha z), \quad (2.13)$$

$$T_{12(21)}(z) = \bar{j} \frac{\kappa_{\text{ac},\mu\nu}(\nu\mu)}{\alpha} \sinh(\alpha z), \quad (2.14)$$

$$\delta = \frac{1}{2}(\kappa_{\text{dc},\nu\nu} + \kappa_{\text{dc},\mu\mu} + \Delta\beta), \quad (2.15)$$

$$\Delta\beta = \beta_\nu + \beta_\mu - \frac{2\pi N}{\Lambda}, \quad (2.16)$$

$$\left| \frac{S(0)}{R(0)} \right|_{S(L)=0}^2 = \left| \frac{-j \frac{\kappa_{\text{ac},\nu\mu}}{\alpha} \sinh(\alpha L)}{\cosh(\alpha L) + j \frac{\delta}{\alpha} \sinh(\alpha L)} \right|^2. \quad (2.17)$$

where $\alpha = j\alpha_{\text{ei}} = \sqrt{|\kappa_{\text{ac}}|^2 - \delta^2}$ is another representation of the eigenvalue. R and S denote the eigenvalue-dependent formula of the guided-mode amplitudes for the reference (forward) and signal (backward), respectively. The detuning parameter $\Delta\beta$ depends on two aspects including the guided-mode propagation constants and the harmonic factor, which is determined by the grating period Λ_{ch} and the harmonic order N , as given in (2.16). In general grating-based structures with non-chirped periods, *i.e.*, $\partial\phi/\partial z = 0$, $N = 1$, and $\Delta\beta = 0$ are employed to evaluate Λ_{ch} for spectral resonance at the desired channel wavelength λ_{ch} .



2.4 Simulation methods

In this section, four solvers/methods are briefly introduced to efficiently design the devices presented in the latter chapters. To evaluate feasibility of a TTAWG, the beam propagation method (BPM), heat transport solver, and FDE solver respectively provided by RSoft and Lumerical are utilized. On the other hand, FDE and finite-difference time-domain (FDTD) are employed to obtain the reflected filtering response of a Bragg grating-assisted structure.

2.4.1 Beam propagation method (BPM)

The main concept of BPM [96] relies on the assumption of dividing electric field $E(x, y, z)$ into two terms including the axially slowly varying envelope term $\phi(x, y, z)$ and the rapid varying phase term $\exp(-jkn_0z)$, where $E(x, y, z)$ satisfies the three-dimensional (3-D) scalar wave equation (Helmholtz equation) expressed by

$$\frac{\partial^2 E}{\partial x^2} + \frac{\partial^2 E}{\partial y^2} + \frac{\partial^2 E}{\partial z^2} + k^2 n^2(x, y, z)E = 0, \quad (2.18)$$

with the electric field $E(x, y, z)$ equivalent to $\phi(x, y, z) \cdot \exp(-jkn_0z)$. By the substitution of E into (2.18), a formula for BPM can be obtained as

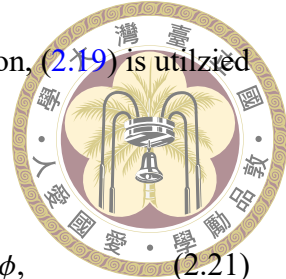
$$\nabla_T^2 - j2kn_0 \frac{\partial \phi}{\partial z} + k^2(n^2 - n_0^2)\phi = 0, \quad (2.19)$$

where ∇_T^2 is an operator expressed as

$$\nabla_T^2 = \frac{\partial^2}{\partial x^2} + \frac{\partial^2}{\partial y^2}. \quad (2.20)$$

To obtain the spatial derivative envelop along the propagation direction, (2.19) is utilized and derived into

$$\frac{\partial \phi}{\partial z} = \frac{-j}{2kn_{\text{EIM}_0}} \frac{\partial^2 \phi}{\partial x^2} - \frac{-jk}{2n_{\text{EIM}_0}} \left[n_{\text{EIM}}^2(x, z) - n_{\text{EIM}_0}^2 \right] \phi, \quad (2.21)$$



where the effective indices n_{EIM_0} and n_{EIM} are the effective indices calculated using effective index method (EIM) to include simulation information within height (y) direction.

In Chapter 3, the BPM provided by RSoft is employed for efficient analysis of the diffractive field as well as beam focusing behavior within the region of two FPRs at different operating wavelengths.

2.4.2 Heat Transport (HT) solver

To evaluate heat transport behavior in terms of external electrical sources, three electrical-related equations should be concerned firstly, including (a) the electrical current equation (Ohm's law), (b) the auxiliary continuity equation, and (c) Gauss' law for DC permittivity ϵ , which can be respectively obtained by

$$\mathbf{J} = \sigma \mathbf{E} = -\sigma \nabla V, \quad (2.22)$$

$$\frac{\partial \rho}{\partial t} = -\nabla \cdot \mathbf{J}, \quad (2.23)$$

$$-\nabla \cdot (\epsilon \nabla V) = \rho, \quad (2.24)$$

where \mathbf{J} , \mathbf{E} , σ , V , ρ , and t denote current density vector, electrical field vector, electrical conductivity, electrical potential, charge density, and time, respectively. For homogeneous

material system, a differential equation can thus be derived into

$$\frac{\partial \rho}{\partial t} + \frac{\sigma}{\varepsilon} \rho = 0.$$



Under the assumption of quasi-static approximation or steady-state, (2.22) combined with (2.23) can then reduce into

$$\nabla \cdot (\sigma \mathbf{E}) = 0. \quad (2.26)$$

On the other hand, a σ -related equation, *i.e.*, power dissipation due to Ohmic loss, can be described by

$$P = \mathbf{J} \cdot \mathbf{E} = \sigma E^2, \quad (2.27)$$

and applied to the heat transport equation as a heat energy transfer rate $Q = P$. While Q can be obtained by

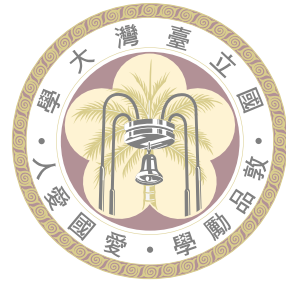
$$Q = m_d C_p \frac{\partial T}{\partial t} - \nabla \cdot (k_c \nabla T), \quad (2.28)$$

where m_d , C_p , T , t , and k_c represent the mass density, the specific heat, temperature, time, and the thermal conductivity, respectively. By solving the last three equations (2.26)–(2.28), the heat transportation behavior can be evaluated. In this dissertation, the heat transport (HT) solver provided by Lumerical is utilized to efficiently analyze the thermal tuning problem.

2.4.3 Finite-difference eigenmode (FDE) solver

To solve eigenmode more efficiently, the commercial finite-difference eigenmode (FDE) solver provided by Lumerical is utilized in the following two chapters. During the simulations, the FD algorithm is employed to mesh the waveguide geometry. Maxwell's equations are then formulated into a matrix eigenvalue problem which is solved by using

sparse matrix technique [97, 98].



2.4.4 Finite-difference time-domain (FDTD) solver

Given that the FDTD method is rigorous solution to Maxwell's equations and widely used for complex geometries, the method is employed in the 3-D simulation of this dissertation. The detailed concept of the FDTD method is given in [99–101], which can be briefly described in the following paragraph.

To demonstrate the concept, four basic Maxwell's equations are considered:

$$\frac{\partial \mathbf{B}}{\partial t} = -\nabla \times \mathbf{E} - \mathbf{M}, \quad (2.29)$$

$$\frac{\partial \mathbf{D}}{\partial t} = \nabla \times \mathbf{H} - \mathbf{J}, \quad (2.30)$$

$$\nabla \cdot \mathbf{D} = 0, \quad (2.31)$$

$$\nabla \cdot \mathbf{B} = 0, \quad (2.32)$$

where \mathbf{E} , \mathbf{D} , \mathbf{H} , \mathbf{B} , \mathbf{J} , \mathbf{M} represent electric field, electric flux density, magnetic field, magnetic flux density, electrical current density, and equivalent magnetic current density, respectively. Note that independent sources of electric ($\mathbf{J}_{\text{source}}$) and magnetic energy ($\mathbf{M}_{\text{source}}$), and loss factors that attenuate both fields via conversion to heat energy, can be introduced into the expressions \mathbf{J} and \mathbf{M} , respectively, as

$$\mathbf{J} = \mathbf{J}_{\text{source}} + \sigma \mathbf{E}; \quad \mathbf{M} = \mathbf{M}_{\text{source}} + \sigma^* \mathbf{H}, \quad (2.33)$$

where σ and σ^* denote electric conductivity and equivalent magnetic loss, respectively, under the condition of linear, isotropic, and nondispersive materials, which can be illus-



(2.34)

trated by

$$\mathbf{D} = \epsilon \mathbf{E} = \epsilon_r \epsilon_0 \mathbf{E}; \mathbf{B} = \mu \mathbf{H} = \mu_r \mu_0 \mathbf{H},$$

with ϵ , ϵ_r , ϵ_0 , μ , μ_r , and μ_0 representing electrical permittivity, relative permittivity, free-space permittivity, magnetic permeability, relative permeability, and free-space permeability, respectively. By the substitution of (2.33, 2.34) into (2.29, 2.30), two Maxwell's curl equations in linear, isotropic, nondispersive, and lossy materials can be derived as

$$\frac{\partial \mathbf{H}}{\partial t} = -\frac{1}{\mu} \nabla \times \mathbf{E} - \frac{1}{\mu} (\mathbf{M}_{\text{source}} + \sigma^* \mathbf{H}); \quad \frac{\partial \mathbf{E}}{\partial t} = \frac{1}{\epsilon} \nabla \times \mathbf{H} - \frac{1}{\epsilon} (\mathbf{J}_{\text{source}} + \sigma \mathbf{E}), \quad (2.35)$$

and then six vector components in Cartesian coordinates can be obtained [100] as

$$\frac{\partial H_x}{\partial t} = \frac{-1}{\mu} \left[\frac{\partial E_z}{\partial y} - \frac{\partial E_y}{\partial z} + (M_{\text{source}_x} + \sigma^* H_x) \right], \quad (2.36a)$$

$$\frac{\partial H_y}{\partial t} = \frac{-1}{\mu} \left[\frac{\partial E_x}{\partial z} - \frac{\partial E_z}{\partial x} + (M_{\text{source}_y} + \sigma^* H_y) \right], \quad (2.36b)$$

$$\frac{\partial H_z}{\partial t} = \frac{-1}{\mu} \left[\frac{\partial E_y}{\partial x} - \frac{\partial E_x}{\partial y} + (M_{\text{source}_z} + \sigma^* H_z) \right], \quad (2.36c)$$

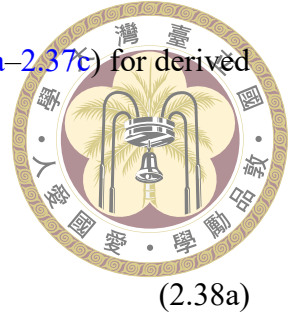
$$\frac{\partial E_x}{\partial t} = \frac{1}{\epsilon} \left[\frac{\partial H_z}{\partial y} - \frac{\partial H_y}{\partial z} - (J_{\text{source}_x} + \sigma E_x) \right], \quad (2.37a)$$

$$\frac{\partial E_y}{\partial t} = \frac{1}{\epsilon} \left[\frac{\partial H_x}{\partial z} - \frac{\partial H_z}{\partial x} - (J_{\text{source}_y} + \sigma E_y) \right], \quad (2.37b)$$

$$\frac{\partial E_z}{\partial t} = \frac{1}{\epsilon} \left[\frac{\partial H_y}{\partial x} - \frac{\partial H_x}{\partial y} - (J_{\text{source}_z} + \sigma E_z) \right]. \quad (2.37c)$$

In 1966 [100], Yee algorithm was proposed to solve for both electric and magnetic fields in time and space using the coupled Maxwell's curl equations instead of only either the electric or magnetic field. Figure 2.2 shows that the three $\mathbf{E}(\mathbf{H})$ components are surrounded by $\mathbf{H}(\mathbf{E})$ components, providing a beautiful and simple way for 3-D space filled by an interlinked array of Faraday's (Eq. 2.29) and Ampere's law (Eq. 2.30) contours. The central differences for the space derivatives and a leapfrog scheme [100] for the time

derivatives for source-free conditions were employed based on (2.36a–2.37c) for derived expressions as



$$H_x|_{i,j+\frac{1}{2},k+\frac{1}{2}}^{n+1} = H_x|_{i,j+\frac{1}{2},k+\frac{1}{2}}^n - \frac{\Delta t}{\mu \Delta y} \left(E_z|_{i,j+1,k+1}^{n+\frac{1}{2}} - E_z|_{i,j,k+1}^{n+\frac{1}{2}} \right) + \frac{\Delta t}{\mu \Delta z} \left(E_y|_{i,j+\frac{1}{2},k+1}^{n+\frac{1}{2}} - E_y|_{i,j+\frac{1}{2},k}^{n+\frac{1}{2}} \right), \quad (2.38a)$$

$$H_y|_{i+\frac{1}{2},j,k+\frac{1}{2}}^{n+1} = H_y|_{i+\frac{1}{2},j,k+\frac{1}{2}}^n - \frac{\Delta t}{\mu \Delta z} \left(E_x|_{i+\frac{1}{2},j,k+1}^{n+\frac{1}{2}} - E_x|_{i+\frac{1}{2},j,k}^{n+\frac{1}{2}} \right) + \frac{\Delta t}{\mu \Delta x} \left(E_z|_{i+1,j,k+\frac{1}{2}}^{n+\frac{1}{2}} - E_z|_{i+1,j,k+\frac{1}{2}}^{n+\frac{1}{2}} \right), \quad (2.38b)$$

$$H_z|_{i+\frac{1}{2},j+\frac{1}{2},k}^{n+1} = H_z|_{i+\frac{1}{2},j+\frac{1}{2},k}^n - \frac{\Delta t}{\mu \Delta x} \left(E_y|_{i+1,j+\frac{1}{2},k}^{n+\frac{1}{2}} - E_y|_{i+1,j+\frac{1}{2},k}^{n+\frac{1}{2}} \right) + \frac{\Delta t}{\mu \Delta y} \left(E_x|_{i+\frac{1}{2},j+1,k}^{n+\frac{1}{2}} - E_x|_{i+\frac{1}{2},j+1,k}^{n+\frac{1}{2}} \right), \quad (2.38c)$$

$$E_x|_{i+\frac{1}{2},j,k}^{n+\frac{1}{2}} = E_x|_{i+\frac{1}{2},j,k}^{n-\frac{1}{2}} + \frac{\Delta t}{\varepsilon \Delta y} \left(H_z|_{i+\frac{1}{2},j+\frac{1}{2},k}^n - H_z|_{i+\frac{1}{2},j-\frac{1}{2},k}^n \right) - \frac{\Delta t}{\varepsilon \Delta z} \left(H_y|_{i+\frac{1}{2},j,k+\frac{1}{2}}^n - H_y|_{i+\frac{1}{2},j,k-\frac{1}{2}}^n \right), \quad (2.39a)$$

$$E_y|_{i,j+\frac{1}{2},k}^{n+\frac{1}{2}} = E_y|_{i,j+\frac{1}{2},k}^{n-\frac{1}{2}} + \frac{\Delta t}{\varepsilon \Delta z} \left(H_x|_{i,j+\frac{1}{2},k+\frac{1}{2}}^n - H_x|_{i,j+\frac{1}{2},k-\frac{1}{2}}^n \right) - \frac{\Delta t}{\varepsilon \Delta x} \left(H_z|_{i+\frac{1}{2},j+\frac{1}{2},k}^n - H_z|_{i-\frac{1}{2},j+\frac{1}{2},k}^n \right), \quad (2.39b)$$

$$E_z|_{i,j,k+\frac{1}{2}}^{n+\frac{1}{2}} = E_z|_{i,j,k+\frac{1}{2}}^{n-\frac{1}{2}} + \frac{\Delta t}{\varepsilon \Delta x} \left(H_y|_{i+\frac{1}{2},j,k+\frac{1}{2}}^n - H_y|_{i-\frac{1}{2},j,k+\frac{1}{2}}^n \right) - \frac{\Delta t}{\varepsilon \Delta y} \left(H_x|_{i,j+\frac{1}{2},k+\frac{1}{2}}^n - H_x|_{i,j-\frac{1}{2},k+\frac{1}{2}}^n \right). \quad (2.39c)$$

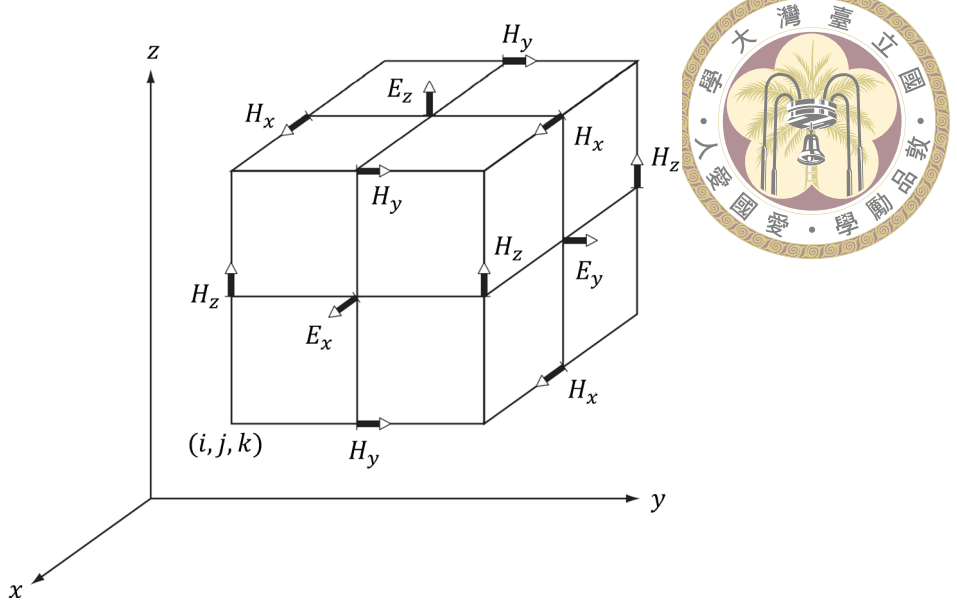


Figure 2.2: Yee's Cell for solving time- and space-dependent electric and magnetic fields.

In summary, the power coupling behavior between electric and magnetic fields obtained from Maxwell's equations over space and time domain can be described within Yee's cell. By using the central differences for the space derivatives and the leapfrog scheme for the time derivatives, six components ($E_x, E_y, E_z, H_x, H_y, H_z$) of both fields at the specific spatial and the temporal grid can be utilized to evaluate the components at the next grid. In this dissertation, the FDTD solver provided by Lumerical [102] is utilized for efficient analysis as well as the visualization of the 3-D electric and magnetic fields.



Chapter 3 Thermally bi-directionally tunable (TBDT) AWG

One of approaches to relaxing the misalignments among the desired channel wavelengths, the filtering channel wavelengths, and the lasing wavelengths is based on the relation between heat and material refractive indices. Although some TTAWGs have been implemented on different platforms [83, 84, 89–92], only one [92] of them was realized for bi-directionally tunable function over thermal mechanism. In the other literature, either red- or blue-shifted spectra alone were achieved with a positive [83, 84, 89] or negative [90, 91] thermo-optic coefficient without compromising the filtering profiles of AWGs. In addition, the required electrical voltage for thermal power are usually several tens of volts [83] for 1–3 W [92] to shift by 2–5 nm due to thermo-optic coefficients of core regions and waveguide dimensions.

In this chapter, a thermally bi-directionally tunable AWG (TBDTAWG) with an ultra-high as well as bi-directionally tuning efficiency is proposed and demonstrated. Moreover, the proposed device was tape-out and implemented with the SiPh platform service provided by Interuniversity Microelectronics Centre (IMEC) for verification. A measurement is carried out 3.3 using the measuring service from Taiwan Semiconductor Research Institute (TSRI). To implement the device with the SiPh platform provided by IMEC, the SOI wafer with a 220-nm-thick silicon layer on a 2- μm -thick buried silicon dioxide interlayer

is utilized in the following designs. Figure 3.1(a)–(c) shows the schematic top view of the proposed TBDTAWG, with Fig. 3.1(d) and 3.1(e) illustrating its crosssection and the magnified portion for clear presentation. The device is composed of two designs which will be presented in the following two subsections, including passive and active ones for realizations of AWG and thermal tuning, respectively.

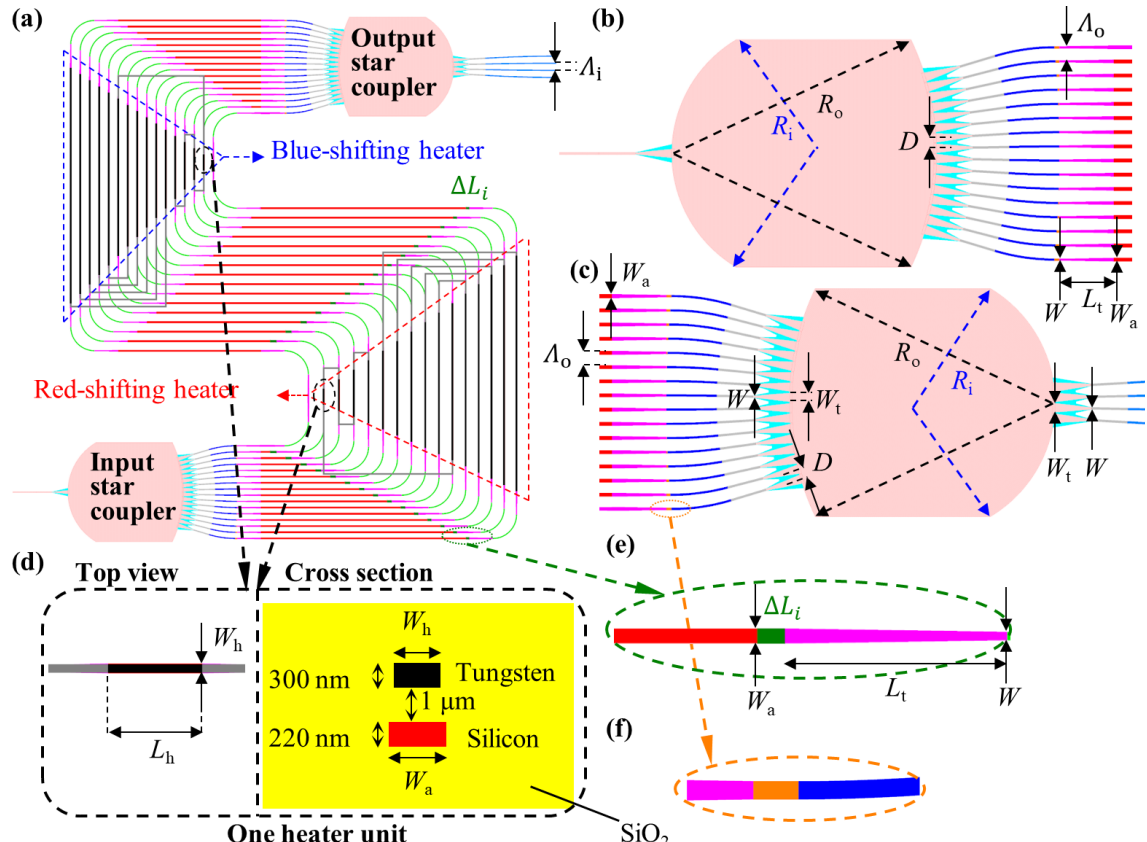


Figure 3.1: Schematic configuration of the proposed S-shaped TBDTAWG.

3.1 Simulation for passive design

The passive design consists of two star coupler and an arrayed-waveguides (AWs) region, for far-field imaging and phase control, respectively. To determine the key parameters, Eqs. (2.1)–(2.7) given in Section 2.1 are utilized in terms of the waveguide dispersive property under the desired configuration. The channel spacing $\Delta\lambda$ of 20 nm is chosen for the O-band CWDM system to relax the misalignments among the desired channel wave-



lengths, the filtering channel wavelengths, and the optical lasing wavelengths. For the single-mode and O-band operations, a core width W of 380 nm is used for the optical input (skin) / output (light blue) ports of the overall device in the arrayed form with a pitch Λ_i of 3 μm , as given in Fig. 3.1. Each star coupler given in Fig. 3.1(b) or 3.1(c) is formed by a FPR with its ports implemented with tapered waveguides based on two levels instead of only singel one, to reduce excess loss (EL) of the filtering response. The two-level tapered waveguide is composed of a 220-nm silicon layer (skin) and a shallow-etched layer (light blue) at its both side walls. The width of the 220-nm silicon layer is linearly tapered between W_t of 1.7 μm and W of 380 nm within a length L_t of 6.67 μm . The arrayed number N_a of 16 for the AWs design is used to cover the mode field diameter (MFD) of the far-field pattern imaged from the input two-level tapered waveguide of the first(input) star coupler. Given the critical dimension of 150 nm of the silicon patterns for the SiPh service provided by IMEC, a pitch D of 1.9 μm is arranged for the ports of the tapered waveguides. To reduce the aberrations, image planes at both star couplers are designed based on the Rowland circle. Radii of shapes for the planes at the slab interfaces with AWs and with input/output ports are denoted by R_o and R_i and assigned 48.64 and 24.32 μm , respectively, using Eq. (2.6), where the channel number $N_{ch} = 6$ instead of 4 is utilized to reduce non-uniformity of the ELs. Regarding the phase difference provided by the AWs, a wider core width W_a of 680 nm is employed to obtain reduced channel crosstalk (XT) suffering from etched wall roughness, *i.e.*, side-wall roughness of waveguides, which is a typical and critical issue for SiPh platform. Under this circumstance, transitions are needed for adiabatic change between the straight waveguides (380 nm) and the wider waveguides (680 nm). Given the utilized wider width, the length difference ΔL_0 of 3.644 μm between the adjacent AWs, and the grating order m of 8 are determined using Eq. (2.5), where the



effective index $n_a(\lambda_0)$ is evaluated using the FDE solver. To provide sufficient spacings for evanescent waves, pitches arrangements $\Lambda_o = 2.6 \mu\text{m}$ and $\Lambda_i = 3 \mu\text{m}$ for AWs and input/output ports, respectively, are chosen, so that S-shaped architecture with complementary phase distributions instead of box-shaped one should be used. To meet the pitch arrangement $\Lambda_o = 2.6 \mu\text{m}$, bent waveguides (BWGs) with designed radii (dark blue) and the connected horizontal waveguides (orange) are utilized, and thus the length difference ΔL_0 should be adjusted for the required phase difference at λ_0 . Fifteen length differences between the adjacent arrayed waveguides are replaced with ΔL_i , which is evaluated on the basis of the effective indices of the BWGs and the horizontal waveguides, where the subscript i denoted the index of array number (1–15). For efficient analysis of the passive design, the simulation for AWG is performed using the 3-D BPM provided by RSoft. In the simulation, a phase correction followed by a 3-D field generation is included between the simulation steps of two star couplers to ensure that the corrected phases contributed by the incremental length differences of AWs are obtained at the entrances of the tapered waveguides. Given the incremental regions implemented with the wider mode, *i.e.*, the fundamental mode of the waveguide width of 680 nm, the default phase correction provided by RSoft is replaced with a user-defined Python function which is called along with other simulation steps under batch command mode. Simulated field distributions at the output star coupler given in Fig. 3.2 showed the feasible function of demultiplexing at four channel wavelengths. In addition, the resulting filtering responses are illustrated in Fig. 3.3, showing that an EL of $\sim 3.6 \text{ dB}$, non-uniformity below 1 dB, and an XT below -20 dB are achieved without considering side-wall roughness.

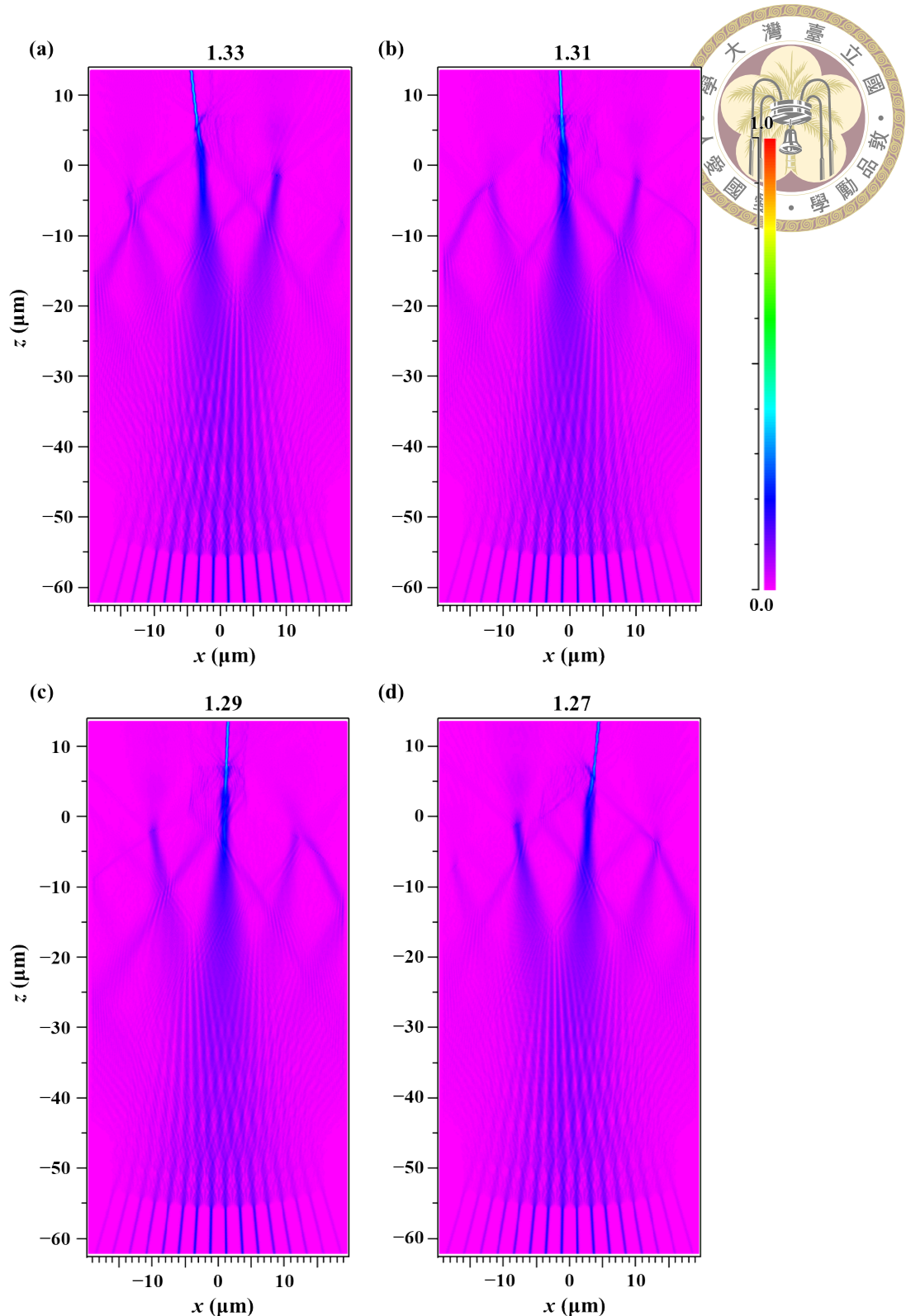


Figure 3.2: Simulated field distributions of the output star coupler operated at four channel wavelengths.



3.2 Simulation for active design

For the active design, a tungsten wire (vertical black traces within dashed triangles in Fig. 3.1) is used as a heater to tune the effective index of the silicon waveguide and consequently shift the filtering response of the AWG. The tungsten wire with a thickness of 300 nm and a width of 600 nm is placed 1 μm above the 220-nm-thick silicon layer. Density of 19300 kg/m³, specific heat of 134 J/kg-K, and thermal conductivity of 173 W/m-K are assumed and assigned to the heat transport properties while a sheet resistance of 650 mW/ \square is used for the electrical property of the tungsten material. To achieve bi-directionally tuning functions and to simplify the tuning issue, two dashed triangular regions with complementary incremental phase shifting contributions in Fig. 3.1(a) are chosen as heating regions. Each triangularly heating region is composed of 120, *i.e.*, $1 + 2 + \dots + (N_a - 1)$, heater units with each unit length of 6.6 μm for both the heating tungsten wire (black) and the heated silicon core (red). All heater units are expected to have the same values of voltage drop and current flow, respectively, in the tungsten wire, providing an equivalent thermal power and thus an equivalent phase shift for all heated units of silicon core. In each triangular region, 120 heater units are divided into 6 parallels, with each parallel consisting of 20 heater units in series to reduce the required electrical voltage for tuning. For example,

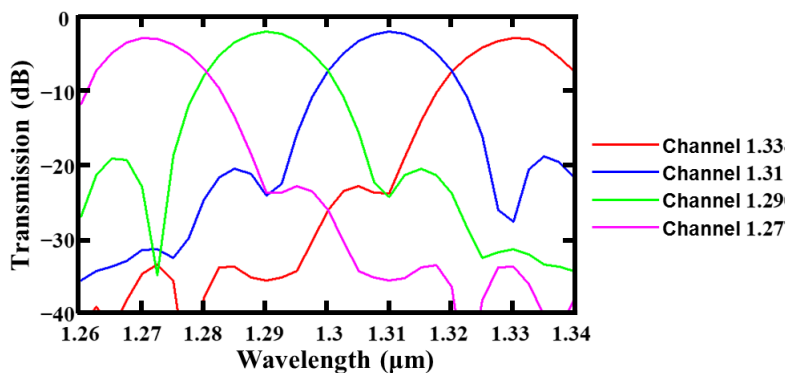


Figure 3.3: Simulated filtering responses of the proposed AWG for the O-band CWDM configuration.



15 heater units inside the 16th arrayed waveguide are connected to 5 heater units inside the 6th one to reach 20 units. Under the arrangement, the thermal crosstalk between heater units is ignored and the simulation for thermal tuning could be simplified to an issue of how much phase shifts can be achieved under different thermal powers provided by each heater unit. The 2-D simulations for the heater unit, shown in the cross-sectional view of Fig. 3.1(d), are performed using both HT and FDE solvers provided by Lumerical Inc. for evaluation of the effective index changes under different unit thermal powers increased from 0 to ~ 2.185 mW. To calculate the spectrum shift $\Delta\lambda$ of the filtering responses of the tuned AWG, an expression obtained by [87]

$$\frac{\Delta L \Delta n_{\text{eff}}}{m} \quad (3.1)$$

is utilized and derived into an equivalent one as

$$\frac{\Delta n_{\text{eff}} \Delta L \lambda_0}{n_{\text{eff}_0} \Delta L_0}, \quad (3.2)$$

where Δn_{eff} and ΔL are parameters for the active design, representing refractive index change and the length difference, respectively, of the heated core, while n_{eff_0} , ΔL_0 , and λ_0 are parameters for the passive design, representing the effective index at the central wavelength, the length difference between adjacent waveguides of the AWs design, and the central wavelength, respectively. Note that the length difference of the heated core ΔL in the expression is the unit length in this design owing to each heater unit consisting of both heating tungsten wire and heated silicon core. Further discussions on tuning performances in terms of the heater unit length are given in Section 3.4. Figure 3.4(a)–(b) illustrates the simulated curves of Δn_{eff} and $\Delta\lambda$ versus required total thermal power P and electrical voltage V_B , respectively, showing a direct proportionality between P and $\Delta\lambda$.



The results show that shifted spectra by approximate 1.51, 6.04, and 9.45 nm are achieved with electrical voltages of 1, 2, and 2.5 V, *i.e.*, total thermal powers of 41.9, 167.8, and 262.2 mW, indicating a linear shift-to-power ratio of $\sim 36.07 \text{ nm/W}$. Given the parallel configuration for heating patterns, the total thermal power P and electrical voltage V_B are obtained by $P = 120 \cdot P_{\text{unit}}$ and $V_B = \sqrt{P_{20 \text{ units}} \cdot R_{20 \text{ units}}}$, respectively, where the subscript “unit” represents one heater unit. The expressions indicate that the required total thermal power P is directly proportional to a unit thermal power P_{unit} while the voltage is proportional to the root of P_{unit} and thus the root of $\Delta\lambda$, as shown in Fig. 3.4(b).

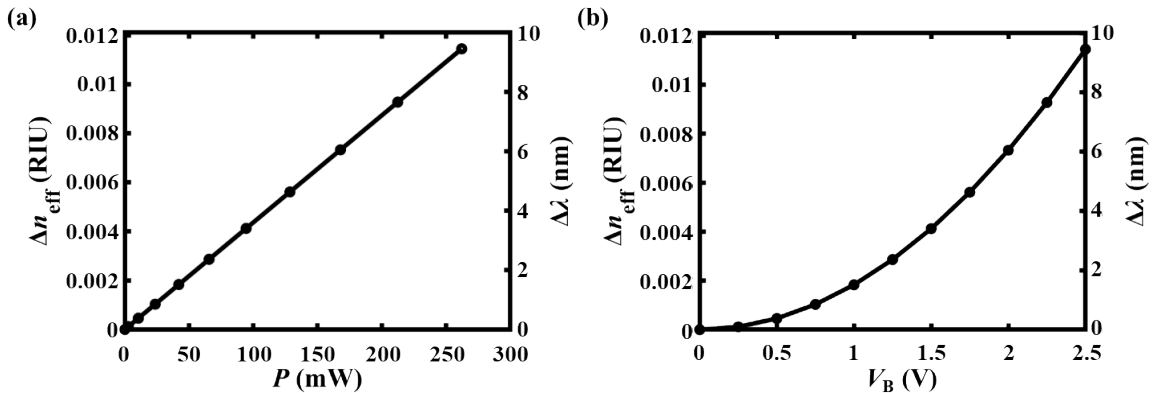


Figure 3.4: Simulated refractive index difference (left y axis) of each heater unit and the corresponding wavelength shifts (right y axis) of filtering response in terms of different (a) thermal powers and (b) applied electrical voltages.

3.3 Measurement results

The proposed TBDTAWG is implemented with the foundry service provided by Interuniversity Microelectronics Centre (IMEC) and measured with a pair of surface grating couplers operated at O-band and TE-polarized state owing to the convenience of surface coupling for measuring and verifying on-chip optical devices. The mask layout of the device is given in Fig. 3.5(a), wherein red and blue regions imply full- and shallow-etched patterns while the white background indicates the non-etched silicon layer. Note that there are dummy patterns being placed above the layer of silicon core to meet the processing

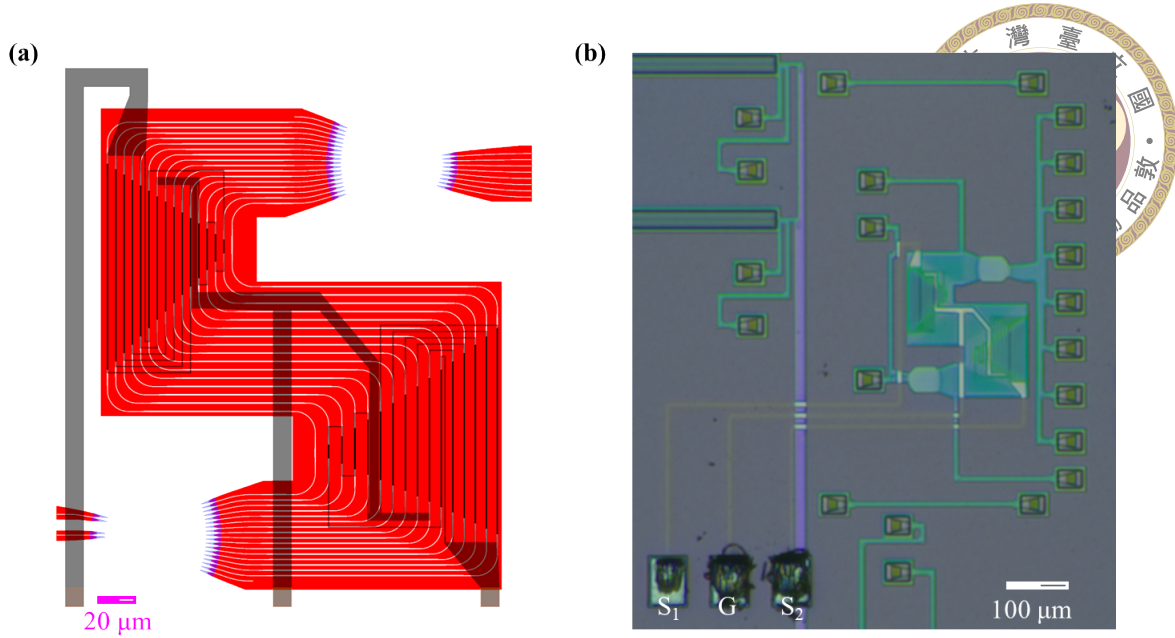


Figure 3.5: (a) Mask layout of the proposed TBDTAWG and (b) photograph of the fabricated device on the SOI chip.

window of the metal layer and to absorb un-guided or scattered light at the white region of the mask layout in the fabrication. However, no dummy patterns should be implemented inside FPRs of both star couplers given that the diffracted lights might be affected due to absorption. To prevent this, a pattern describing a region without dummy patterns is defined and covered on the entire AWG. In Fig. 3.5(b), the dark-gray region outside the AWG comes from the dummy patterns while the non-etched silicon regions such as FPRs and waveguides are visible with a lighter color. In the fabricated device, an additional input and four output ports are employed at two corresponding star couplers for autocorrection of the filtering responses by red- or blue-shift tuning in terms of the optical transmissions in the middle two of these extra output ports for Channels 1.29 and 1.31, *i.e.*, two channels adjacent to the central wavelength of 1.3 μm, if a low-power input source operated at 1.3 μm is introduced. Detailed concepts for monitoring process will be given in the next section. In Fig. 3.5(a), the vertical black strips illustrate the heating tungsten wires connected for 6 parallels with each parallel consisting of equivalent 20 heater units to reduce the required tuning voltages. The electrical connections are re-

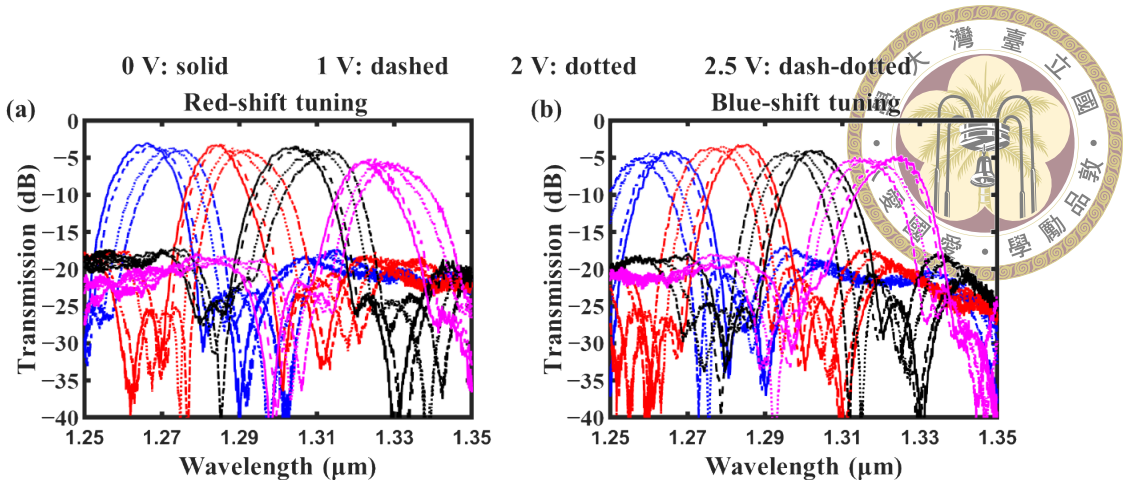
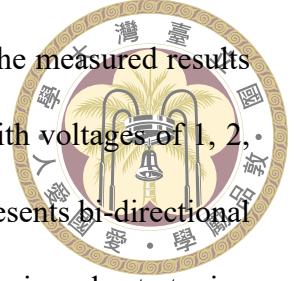


Figure 3.6: (a) Red-shifted and (b) blue-shifted filtering responses for different applied voltages V_B of 0, 1, 2, and 2.5 V are represented by solid, dashed, dotted, and dash-dotted lines, respectively.

alized with metal patterns in dark gray, as shown in Fig. 3.5(a), and a pad configuration of S_1GS_2 with a pitch of 100 μm . Under these arrangements, red-shifted spectra can be obtained with electrical voltages applied on GS_2 while blue-shifted ones can be measured with S_1G . Figure 3.6(a) and (b) show the measured results of red- and blue-shifted spectra, respectively, under electrical voltages of 0, 1, 2, and 2.5 V which correspond to the solid, dashed, dotted, and dash-dotted lines, respectively. An EL and XT of approximate 4 dB and -15 dB, respectively, are given in the figures. Compared to simulated spectrum given in Fig. 3.3, the measured EL for the passive design is increased by less than 1 dB, which could be attributed to side-wall-roughness losses due to (a) multi-mode excitations at the interfaces between tapered waveguides and FPRs and/or (b) inevitable waveguide couplings when modes exit/enter FPRs and enter/exit AWs. Some efforts discussed in the next section can be made to address the issue. In addition, the measured XT of the passive design is increased by ~ 5 dB, which could be due to phase errors resulting from inaccurate incremental phase differences or the side-wall roughness contributed by the arrayed waveguides. The measured spectra also imply that the thickness of 220-nm silicon layer might be deviated by a small amount, resulting in a blue shift of 7 nm for the passive design. A proper silicon thickness of 215 or 210 nm for simulation might lead to a bet-



ter agreement with the measured results. For tuning performances, the measured results show that spectrum shifts of ± 1.4 , ± 5.5 , and ± 8 nm are achieved with voltages of 1, 2, and 2.5 V, respectively, for each channel, where the symbol “ \pm ” represents bi-directional tuning functions. The results also show that differences of channel spacings due to tuning are less than 1.2 nm under these voltages, indicating a good shifting feature of the device. In addition, nonsignificant EL and XT differences in terms of tuning shown in Fig. 3.6 could be attributed to a thermally induced misalignment between the fiber and the chip due to the thermal expansion of the chip during the measurement. Fortunately, this issue could be resolved by permanently bonding the input/output fibers to the chip. Note that XTs are much more sensitive to phase errors when compared to ELs. Inaccurate thermal tunings of incremental phase shifts of arrayed waveguides will significantly increase XTs which are not observed in the measured result. Comparisons between simulated (black curve) and measured (red square) results are given in Fig. 3.7(a)–(d) and 3.7(e)–(h) for red- and blue-shifted spectra, respectively, at each channel, showing a good agreement

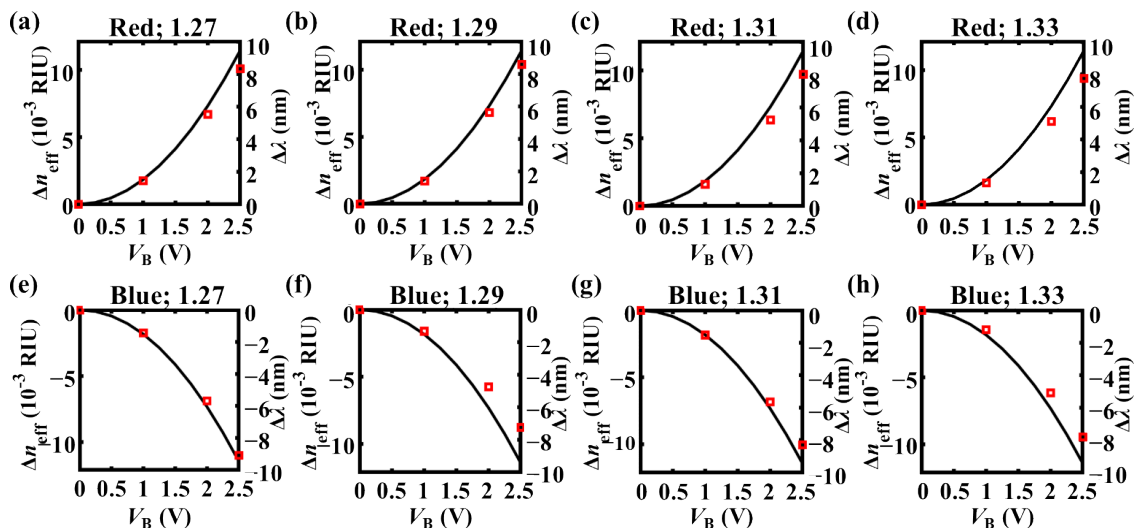


Figure 3.7: Effective index differences (left y axis) of adjacent AWs and wavelength shifts (right y axis) of filtering response in terms of electrical voltages at four output Channels 1.27, 1.29, 1.31, and 1.33 μm for (a–d) red-shift tuning and (e–h) blue-shift tuning, where the solid line and squared red marker represent the simulated results from Fig. 3.4 and the measured data from Fig. 3.6, respectively.

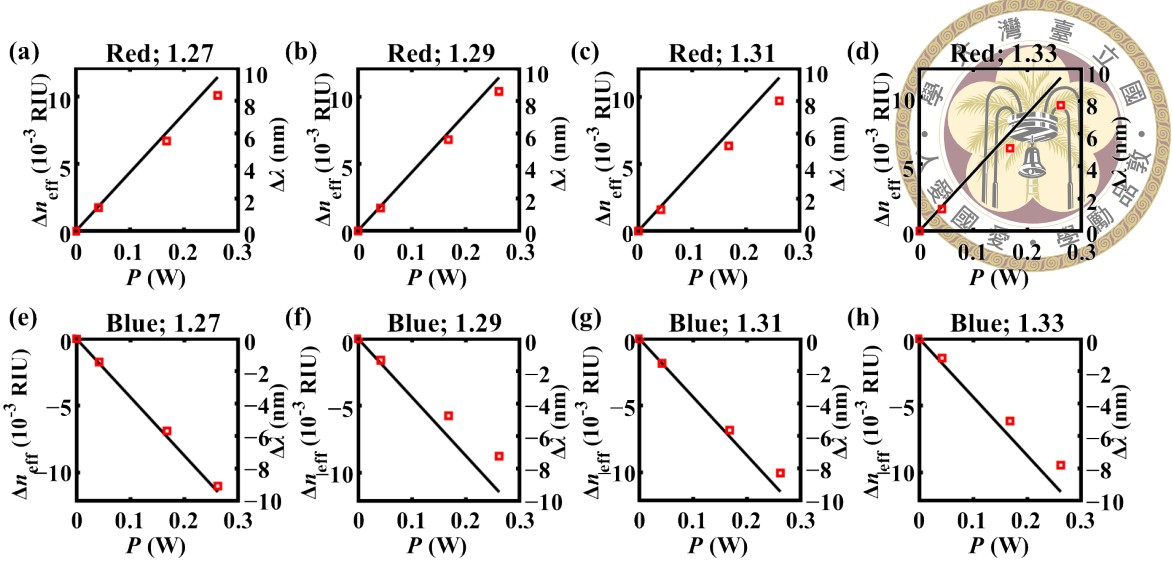
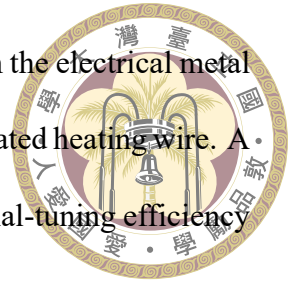


Figure 3.8: The linear relationship between the spectrum shifts and the required thermal powers at four output Channels 1.27, 1.29, 1.31, and 1.33 μm for (a–d) red-shift tuning and (e–h) blue-shift tuning, where the solid line and squared red marker represent the simulated results from Fig. 3.4 and the measured data from Fig. 3.6, respectively.

between simulation and measurement, and indicating the feasible functions of thermally bi-directional tuning for the proposed device. Moreover, Fig. 3.8 illustrates a direct proportionality, as shown in Fig. 3.4(a), between total thermal powers P , *i.e.*, 120 units of P_{unit} , and spectrum shifts $\Delta\lambda$. For a total thermal power P of 262 mW, an index change Δn_{eff} of ± 0.0114 and a shift $\Delta\lambda$ of $\pm 8 \text{ nm}$ are obtained from the measured results, indicating a linear bi-directional shift-to-power ratio of $\pm 30.5 \text{ nm/W}$ with a wide tuning range of 8 nm. The difference of absolute values of linear ratios between simulation (36.07 nm/

Table 3.1: Thermal-tuning performance comparison of thermally tunable AWGs in the literature.

Literature	Tuning efficiency	Tuning direction	Applied voltage	Tuning range	Platform	TO coefficient
2020 [83]	6.4 nm/W	Red	40 V for 2.3-nm shift	2.5 nm	Silicon	$1.68 \cdot 10^{-4} / \text{K}$
2015 [84]	~ 3.97 nm/W	Red	40 V for 5-nm shift	5 nm	Silicon; SiO_2	$1.84 \cdot 10^{-4} / \text{K}; 1 \cdot 10^{-5} / \text{K}$
1999 [90]	–	Blue	–	9 nm	Polymer	$-1.6 \cdot 10^{-4} / \text{K}$
2006 [91]	–	Blue	–	6.6 nm	Polymer/Si	$-1.16 \cdot 10^{-4} / \text{K}$
1999 [92]	± 2 nm/W	Bi-directional	–	6 nm	SiO_2 -Si	positive
Proposed Device	± 30.5 nm/W	Bi-directional	2.5 V for ± 8-nm shift	$\geq 8 \text{ nm}$	Silicon	$1.68 \cdot 10^{-4} / \text{K}$



W) and measurement (30.5 nm/W) might come from the power loss in the electrical metal traces or from a deviated thickness and/or sheet resistance of the fabricated heating wire. A performance comparison is given in Table 3.1, showing a better thermal-tuning efficiency with bi-directional tuning functions for the proposed device.

3.4 Discussion

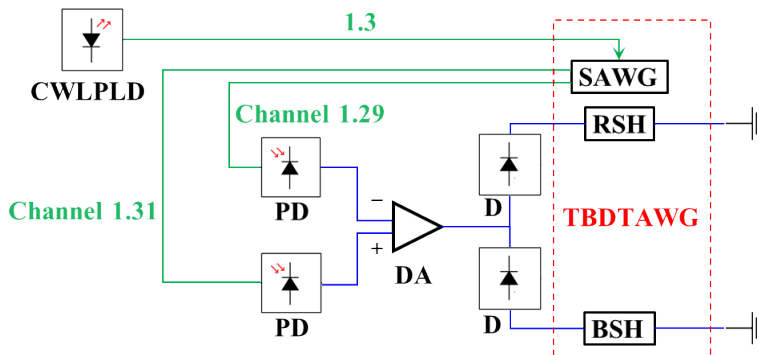


Figure 3.9: Scheme for automatically stabilizing the spectral responses of thermally bi-directionally tunable AWG for WDM communication systems. CWLPLD, continuous-wave low-power laser diode; SAWG, S-shaped arrayed waveguide grating; PD, photodiode; DA, electrical differential amplifier; D, diode; RSH, red-shifting heater; BSH, blue-shifting heater; TBDTAWG, thermally bi-directionally tunable arrayed waveguide grating. Green and blue routing wires represent optical and electrical connections, respectively.

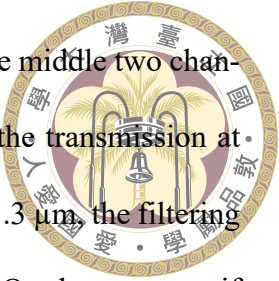
From the simulated and measured ($V_B = 0 \text{ V}$) spectrum shown in Figs. 3.3 and 3.6, respectively, slightly higher ELs and XTs are obtained for the passive design of the fabricated device, as mentioned in the former section. The higher EL of the passive design might come from sidewall-roughness loss due to multi-mode excitations and/or inevitable waveguide couplings near the interfaces between AWs and FPRs, where a tip width of $1.9 \mu\text{m}$ is used for the tapered waveguides. To reduce the EL, a mono-mode condition as well as the best coupling length for tapered waveguides with shallow-etched patterns in junction with FPRs proposed in [103] could be utilized. On the other hand, the increased XT of the passive design could be attributed to phase errors due to length difference errors between adjacent AWs as well as fabricated side-wall roughness at the bending waveg-



uides. For a better agreement with the simulated passive spectrum, snapping patterns to integer points on mask layout without compromising simulated spectra and using improved fabrication processes might be helpful.

Given that both triangular regions with complementary incremental phase shifting contributions for active tuning are implemented outside two regions, which determine passive filtering responses, with modified incremental length differences of arrayed waveguides, a longer/shorter unit length can be realized with a larger/smaller pitch of arrayed waveguides at the upper one of two incremental passive regions determined by the modified length differences ΔL_i . Although a longer/shorter unit length can be achieved, a smaller/larger thermal power would be obtained under the same electrical voltage, leading to the same linear shift-to-power ratio as the one before using different unit length. The reason comes from the relation (direct proportionality) between the heating length, *i.e.*, the length of each heater unit, and the tungsten resistance of each heater unit. The longer/shorter unit length is used in the device, the larger/smaller unit resistance would be obtained, resulting in a reduced/increased spectrum shift and thermal power by a simultaneous ratio under the same electrical voltage and thus the same linear shift-to-power ratio. In other words, a wider tuning range under the same electrical voltage can be implemented with a shorter unit length while no differences of linear shift-to-power ratio, which comes from material properties, would be made.

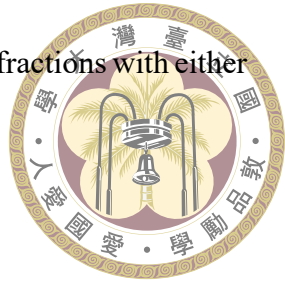
To implement a function for automatically stabilizing the filtering responses, *i.e.*, thermally bi-directional tuning the spectral responses automatically until the condition is stabilized, a scheme employing an additional input port for a central wavelength and four extra output ports for the corresponding channels is proposed in Fig. 3.9. In this scheme, a low-power optical source operating at the central wavelength of 1.3 μm is utilized and



introduced into the additional input port to monitor transmissions in the middle two channels, *i.e.*, Channels 1.29 and 1.31, of the additional output ports. If the transmission at Channel 1.29 is higher than the one at Channel 1.31 when operated at $1.3\text{ }\mu\text{m}$, the filtering responses of the AWG should be blue-shifted for the WDM system. On the contrary, if the comparison result is reversed, then the spectral responses of the device should be red-shifted. Because the speed of thermal conduction might be less than the one of voltage change that is controlled by the feedback loop, a proper proportional integral derivative (PID) control [44] can be applied to the feedback control circuit so that the stable condition of $T_{1.29}(1.3\text{ }\mu\text{m}) = T_{1.31}(1.3\text{ }\mu\text{m})$ is satisfied. Here $T_{\lambda_{\text{ch}}}(\lambda_0)$ represents the transmission at the monitoring port for Channel λ_{ch} when operated at the wavelength of λ_0 . Note that the PID control should be carefully optimized to compensate for the environmental thermal loss and to avoid temperature oscillation before the stable condition occurs so that the amplified differential voltage is in the range of 1–2 V.

Considering the system signals and monitoring low-power optical source are both introduced into the device using the corresponding input ports when demultiplexing, the low-power source operated at $1.3\text{ }\mu\text{m}$ at the monitoring ports for Channels 1.31 and 1.29 will result in the spatial diffraction with lower ($m - 1$) order to the system port for Channel 1.33 given the designed FSR of 6 channel spacings and the monitoring input port being placed 4 channel spacings away from the system input port in the layout. On the other hand, the higher ($m + 1$) order of the $1.33\text{-}\mu\text{m}$ signal at the system port for Channel 1.33, *i.e.*, the upper-right focused beam shown in Fig. 3.2(a), could also affect the monitoring one for Channel 1.29. However, the issue can be easily addressed with two solutions including: (a) using a wider FSR of 7 or 8 channel spacings at the expense of larger footprint of the entire device, or (b) placing the monitoring input port 3 instead of 4 channel

spacings away from the system input port, so that XTs due to spatial diffractions with either the higher ($m + 1$) or the lower ($m - 1$) order can be avoided.



3.5 Summary

A thermally bi-directionally-tunable (TBDT), namely both red- and blue-shift tunable, arrayed waveguide grating (AWG) was proposed and demonstrated based on 193-nm lithographic complementary-metal-oxide-semiconductor (CMOS) technology. The device was composed of passive and active designs for realization of an AWG and fine tuning of its filtering responses, respectively. By leveraging an S-shaped architecture for the passive design and six parallel components with each one consisting of twenty equivalent heater units in series for the active one, a thermally bi-directionally tunable AWG (TBDTAWG) applied with ultra-low electrical voltages for wide spectrum shift can be achieved. An even wider tuning range can be realized with a shorter length of the heater unit without compromising the shift-to-power ratio or tuned/untuned spectra if sufficient spacings are provided for evanescent waves of arrayed waveguides. Measurement results show that both red- or blue-shifted spectra can be achieved and a linear bi-directional shift-to-power ratio of ± 30.5 nm/W as well as a wide tuning range of ~ 8 nm can be obtained under an electrical voltage range of 0–2.5 V. This shows a good agreement with simulation data and highlights a great potential for the proposed device to deal with fabrication errors and environmental temperature change.



Chapter 4 Bragg grating-assisted WDM filter

To relax misalignments among desired channel, optical lasing, and filtering channel wavelengths due to increased environmental temperature and fabrication errors, some coarse wavelength division (de)multiplexing (CWDM) systems that utilize large channel spacings have been proposed and their capability has already been demonstrated [10, 34–38, 40–61, 104]. To broaden the available channel bandwidth (ABW) under the desired low crosstalk (XT) to further improve the communication system, flattened filtering responses are required.

In this chapter, an elegant approach to flattening responses is based on the Bragg grating structure (BGS) to achieve low-EL, highly uniform, and flat-top responses [40–45]. A rectangular response was obtained in [41] with a sinusoidal-profile contra-directional coupling coefficient κ_{ac} by using both amplitude and phase apodizations along the propagation direction. In the literature, the amplitude apodization was achieved using simple tapered waveguides as transitions at the beginning and at the end of a multi-mode waveguide Bragg grating (MMWBG), whereas the phase apodization was obtained by relatively shifting one of the two side-wall BGSs, *i.e.*, width corrugations, along the propagation direction. These led to a sub-decibel EL and low XT below –20 dB to the high side-lobe suppression ratios (SLSRs) and near-perfect box-like filtering responses. The silicon-based

WBGs, however, were critically dimensioned at 125 nm for the channel wavelength of 1.271 μm by using electron beam lithography. Furthermore, the presented grating periods for four channel wavelengths had drifted from the calculated Bragg periods by ~ 20 nm due to the non-zero dc-shift term “ δ ” derived in the perturbed-permittivity CMT (PPCMT) [1]; thereby significantly increasing the difficulty of designing such devices and resulting in unbalanced side-lobe suppression at both sides of resonant wavelengths “ λ_r ”, *i.e.*, low side-lobe imbalance (SLI) as defined in Section 4.1. By contrast, XTs can also be further reduced by engineering both amplitude and phase apodizations using Gaussian-like profiles simultaneously. Although this would be at the cost of a slightly higher 20-dB spectral bandwidth (BW_{20-dB}), such a tradeoff is still acceptable for a CWDM system with a 20-nm channel spacing.

4.1 Device structure and optimization

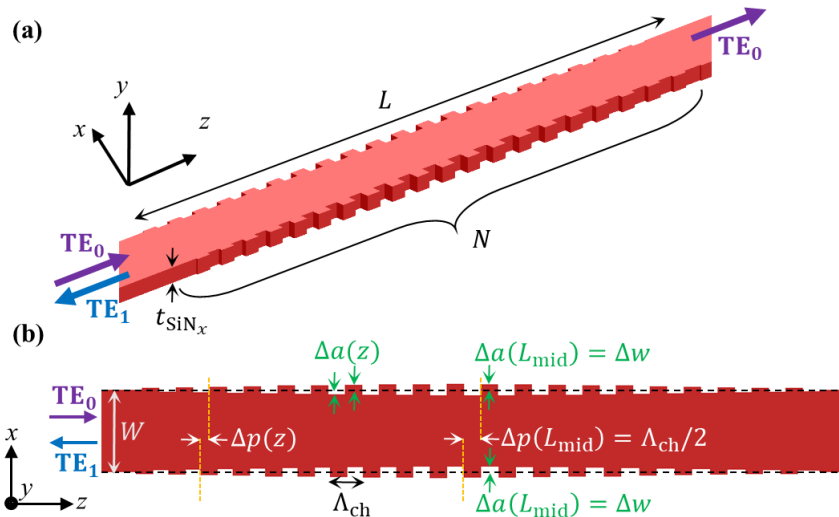


Figure 4.1: Schematic (a) 3-D and (b) top views of the proposed MMWBG.

Figure 4.1 shows the schematic diagrams of the proposed MMWBG that uses a 400-nm-thick silicon-nitride layer for each of the four channels over an SOI platform. The silicon-nitride layer is placed 400 nm above the 220-nm-thick silicon layer of the SOI

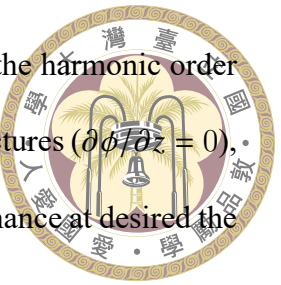


wafer, to meet the available SiPh foundry service. Each MMWBG is composed of a multi-mode waveguide and corrugations at both side walls of the waveguide such that the forward TE_0 mode can be contra-directionally coupled into the backward TE_1 mode with the filtering response shape of a hyperbolic-tangent function. The reflected TE_1 -mode signal is designed to be dropped using a broadband and high-efficiency TE_1-TE_0 asymmetric directional coupler. Circulators for protecting the optical source from reflected signals is not required under this arrangement. To more efficiently determine the required Bragg periods for resonance at the desired channel wavelengths λ_{ch} , perturbed-permittivity CMT principle was utilized. The differential equations of the counter-propagating perturbed-permittivity CMT [1] were minimally adjusted and are given in (2.8)–(2.11), where z is the spatial position along the propagation direction, A and B represent the transverse guided-mode amplitudes, and v and μ denote the forward and backward propagation modes, respectively. The parameters ω , ε_0 , and $\varepsilon_{r,(\text{dc},\text{ac})}$ represent the angular frequency determined by the optical wavelength, the permittivity of free space, and the perturbation profile of the relative permittivity constant, respectively. The wavelength-dependent parameters κ , $\Delta\beta$, and ϕ are the coupling coefficient, phase mismatch (detuning), and spatially varying phase change, respectively. The coupling coefficients κ_{dc} and κ_{ac} are obtained by the overlap integration in terms of the dc and ac terms of the permittivity perturbation profile, respectively, and the modes involved in the coupling, whereas \mathbf{E} denotes the normalized transverse electric fields of the guided modes, as given in (2.10) and (2.11). The expressions in (2.12)–(2.17) describe the contra-directional coupling behavior over a transfer matrix, where α equals $\sqrt{|\kappa_{\text{ac}}|^2 - \delta^2}$, and R and S are eigenvalue-dependent representations of the guided-mode amplitudes for the reference (forward) and signal (backward), respectively. The detuning parameter $\Delta\beta$ depends on the guided-mode propagation con-

stants and the harmonic factor decided by the grating period Λ_{ch} and the harmonic order N , as expressed in (2.17). In general cases for non-chirped grating structures ($\partial\phi/\partial z = 0$), $N = 1$ and $\Delta\beta = 0$ are employed to determine the required Λ_{ch} for resonance at desired the channel wavelength λ_{ch} .

The resonant wavelength λ_r , *i.e.*, the wavelength with the maximum reflected signal spectral transmission, can deviate away from the desired channel wavelength λ_{ch} due to the non-zero dc-shift term δ , which is the non-zero sum of the two coupling coefficients $\kappa_{\text{dc},vv}$ and $\kappa_{\text{dc},\mu\mu}$ obtained in (2.15). Note that an adjustment is made in (2.15) to cater to the reflected guided TE₁ mode denoted by $\kappa_{\text{dc},\mu\mu}$. In (2.17), the reflected signal at λ_r is obtained by the assumption of no reflected signal amplitude at the end of WBG, *i.e.*, $S(L) = 0$, where L is the full length. From this expression, the maximum transmission of $|\tanh(\alpha(\lambda_r)L)|^2$ can be achieved with $\delta(\lambda_r) = 0$. For efficient design of such device, the condition $\lambda_r = \lambda_{\text{ch}}$ should be met so that only the information of guided-mode effective indices and λ_{ch} are required to evaluate the Bragg period.

To meet the condition, $\delta(\lambda_{\text{ch}}) = 0$, namely $\kappa_{\text{dc},vv} = \kappa_{\text{dc},\mu\mu} = 0$, is engineered with a tailored width for the multi-mode waveguide. A core width of the MMWBG is chosen to achieve approximately identical positive and negative index changes in terms of identical width variation for the TE₀ and TE₁ modes, respectively. In addition, to guide both the TE₀ and TE₁ modes and to achieve shorter length of the TE₁-mode dropping device, which is presented in following paragraphs, the core width allowing for smaller TE₁-mode effective indices with lower confinements at the four channel wavelengths is utilized. A relation between the TE-mode effective indices and the core widths is characterized in Fig. 4.2 using the FDE solution (Lumerical Inc.) to determine the appropriate width. Based on the curve shown in Fig. 4.2, the core width of 950 nm and the corrugated structure for



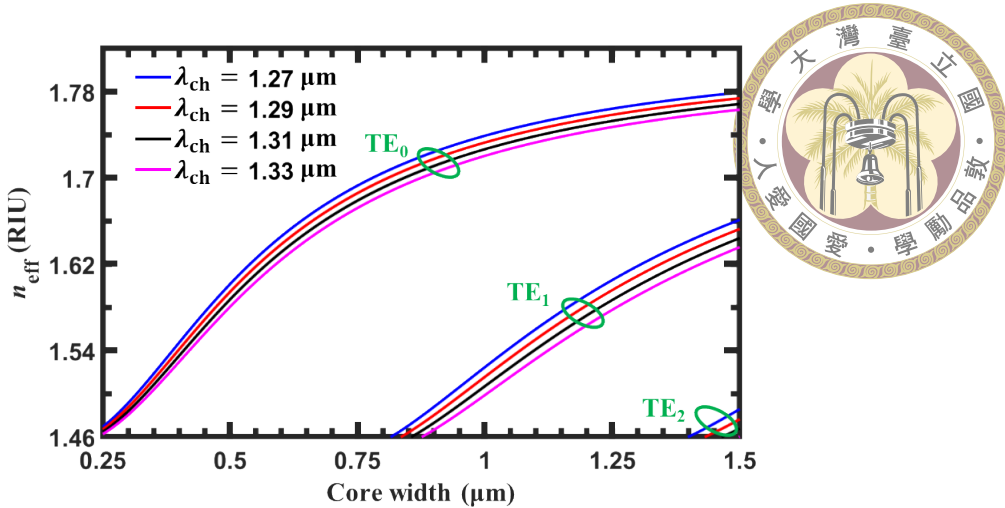


Figure 4.2: Effective refractive indices of the first three TE modes versus core widths for four channel wavelengths.

Table 4.1: Required Bragg periods for the four-channel CWDM system.

λ_{ch} (μm)	1.27	1.29	1.31	1.33
Λ_{ch} (nm)	392	400	408	416

the amplitude apodization shown in Fig. 4.1(b) are determined to satisfy $\lambda_r = \lambda_{\text{ch}}$, and consequently the required Bragg period for resonance can be simply evaluated using the phase matching condition $\Delta\beta = 0$, or an equivalent expression of $\Lambda_{\text{ch}} = \lambda_{\text{ch}} / (n_{\text{eff}}^{\text{TE}_1} + n_{\text{eff}}^{\text{TE}_0})$ as given in Table 4.1.

For an ultra-low XT leveraging the spatial Fourier transform, both amplitude and phase apodizations are applied on the corrugated width to obtain $\kappa_{\text{ac}}(z)$ with a sinusoidal profile. The expressions obtained by

$$\Delta a(z) = \Delta w \cdot \exp \left(- \left(\frac{z - L_{\text{mid}}}{L/\sqrt{s_a}} \right)^2 \right) \text{ and} \quad (4.1)$$

$$\Delta p(z) = \frac{\Lambda_{\text{ch}}}{2} \cdot \exp \left(- \left(\frac{z - L_{\text{mid}}}{L/\sqrt{s_p}} \right)^2 \right) \quad (4.2)$$

illustrate the amplitude apodization $\Delta a(z)$ and phase apodization $\Delta p(z)$, respectively, where $\Delta a(L_{\text{mid}}) = \Delta w$ and $\Delta p(L_{\text{mid}}) = \Lambda_{\text{ch}}/2$ are used to achieve the maximum value of κ_{ac} at half of the full length, *i.e.*, $z = L_{\text{mid}} = L/2$. For simplification, the apodization strengths s_a and s_p in (4.1) and (4.2), respectively, are assigned the same value s under a

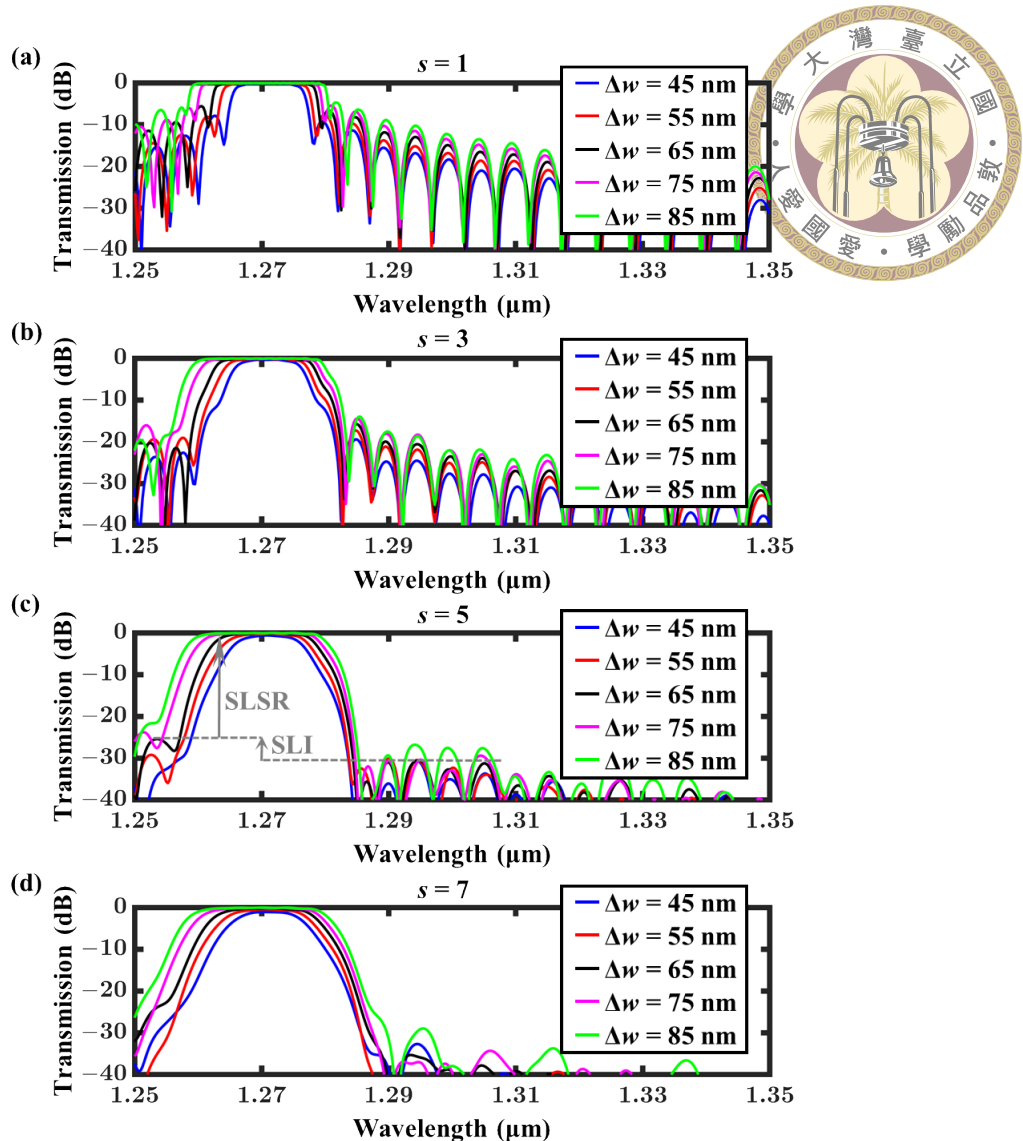
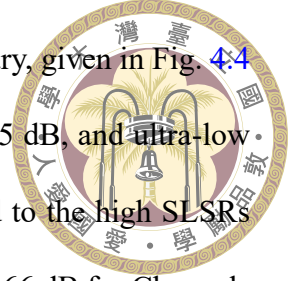


Figure 4.3: Simulated filtering responses using 3-D FDTD method for $\lambda_{ch} = 1.27 \mu\text{m}$ in terms of $\Delta_{ch} = 392 \text{ nm}$ and different maximum width corrugations Δw .

fixed duty cycle of 0.5. Figure 4.3 depicts the simulated filtering responses using the 3-D FDTD method (Lumerical Inc.). The calculated period of 392 nm (Table 4.1) is utilized in a 3-D model for resonance at the channel wavelength λ_{ch} of 1.27 μm . Both apodizations are employed at different Δw ranging from 45 to 85 nm in a step of 10 nm and s ranging from 1 to 7 in a step of 2. For a flat-top response with a 1-dB channel BW ($BW_{1-\text{dB}}$) of 14 nm and SLI as defined in Fig. 4.3(c) that remains below 5 dB while the SLSR remains above 25.5 dB, the parameter set ($\Delta w, s$) of (65 nm, 5) is utilized in the following simulations. The filtering responses of the four individual MMWBGs, which are critically



dimensioned at 196 nm and achievable at a representative SiPh foundry, given in Fig. 4.4 show that ultra-low ELs below 0.3 dB, high uniformity above -0.035 dB, and ultra-low-XTs below -25.5 dB are achieved. The ultra-low XTs are attributed to the high SLSRs above 25.5 dB, and the low SLIs of approximately 2.5, 4.63, 6, and 6.66 dB for Channels 1.27, 1.29, 1.31, and 1.33 μm , respectively. Moreover, the available bandwidth for XTs below -25 dB ($\text{ABW}_{25-\text{dB}}$) reaches 13.5 nm, which is beneficial for performances of the overall CWDM filter.

To drop the reflected TE_1 -mode signal using four identical devices at the corresponding channels, a broadband asymmetrical directional coupler (BADC) based on silicon nitride over the SOI platform is designed at the entrance of each MMWBG. Under this arrangement, its fabrication tolerance analysis is not necessary given that broadband devices usually allows for low sensitivity to geometry, if the devices are sufficiently large. In addition, the mesh accuracy required for the BADC simulation can be significantly reduced owing to the broadband performance as well as the lower sensitivity to geometry, greatly saving the demanded optimization time using a user-defined algorithm. Figure 4.5 shows the schematic top view of the BADC, with the input/through and cross ports carrying the counter-propagating TE_1 and TE_0 modes, respectively. The design methodology proposed in [67] is utilized for an optimization using the 3-D FDTD method in combination with a user-defined adaptive particle swarm algorithm APSO [105] to obtain high coupling efficiencies in the given wavelength span. To guide at the two lowest modes obtained in Fig. 4.3 and to achieve an adiabatic coupling at the region within the length denoted by L_1 , W_{t_2} and W_{c_1} are fixed at the core width 860 nm and the critical dimension 150 nm, respectively, while the remaining parameters given in Fig. 4.5 optimized using the user-defined APSO. Table 4.2 lists the optimal parameter set to achieve a broadband

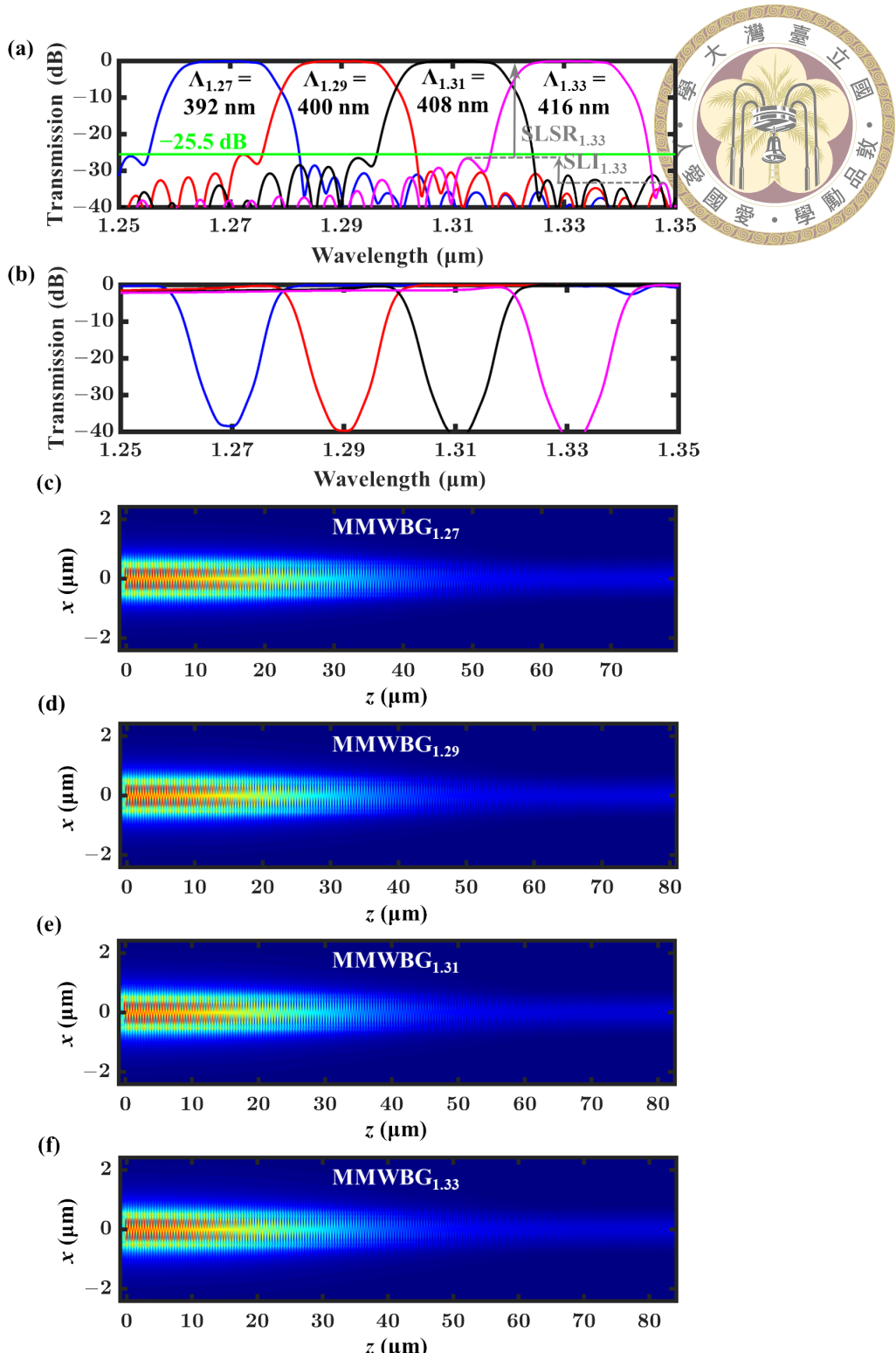


Figure 4.4: Simulated filtering responses of (a) the contra-directional coupled TE_1 mode, (b) the remaining forward TE_0 mode, and (c)–(f) the electric-field top-view profiles at the given four channel wavelengths, respectively, for the corresponding individual MMWBGs using the 3-D FDTD solutions in terms of the parameter set $(W, \Delta w, s) = (950 \text{ nm}, 65 \text{ nm}, 5)$.

coupling response from the TE_1 mode at the input/through port to the TE_0 mode at the cross port. The simulated transmission and spectral response of the extinction ratio (ER)

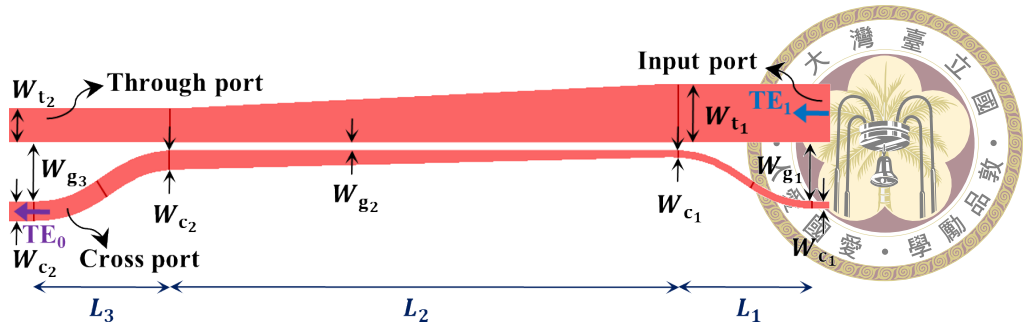


Figure 4.5: Schematic top view of the SiN_x -based BADC for broadband coupling from the TE_1 mode at through port to the TE_0 mode at cross port.

Table 4.2: Optimal parameter set of SiN_x -based BADC.

Parameter	W_{t_1}	W_{t_2}	W_{c_1}	W_{c_2}
Value (μm)	1.305	0.86	0.15	0.395
Parameter	W_{g_1}	W_{g_2}	W_{g_3}	
Value (μm)	1.145	0.23	0.36	
Parameter	L_1	L_2	L_3	
Value (μm)	29.335	80.785	34.94	

between the TE_0 and TE_1 modes are respectively depicted in Fig. 4.6(a) with blue and red curves, where the ER is defined as

$$\text{ER} = 10 \cdot \log_{10} \left(T_{\text{TE}_0}^{\text{cross}} / T_{\text{TE}_1}^{\text{through}} \right), \quad (4.3)$$

with electric-field profiles at corresponding wavelengths given in Fig. 4.6(b)–(g). From the results, the TE_1 – TE_0 coupling ratios above 98.63 % (> -0.06 dB) and ultra-high ERs above 40 dB are achieved within the wavelength span of 1.25–1.35 μm , demonstrating the feasibility of dropping the TE_1 mode efficiently without compromising the filtering responses of the MMWBGs. Note that a high fabrication tolerance of the BADC can be reasonably assumed so that only the tolerance of the MMWBGs are analyzed in the following section, owing to (i) the low-index contrast in terms of the core (silicon nitride) and cladding (silicon dioxide) materials, (ii) the ultra-high and broadband coupling efficiency, and (iii) the large footprint of the BADC. To evaluate the performances of the overall O-band CWDM filter, four groups for the corresponding channels are cascaded in

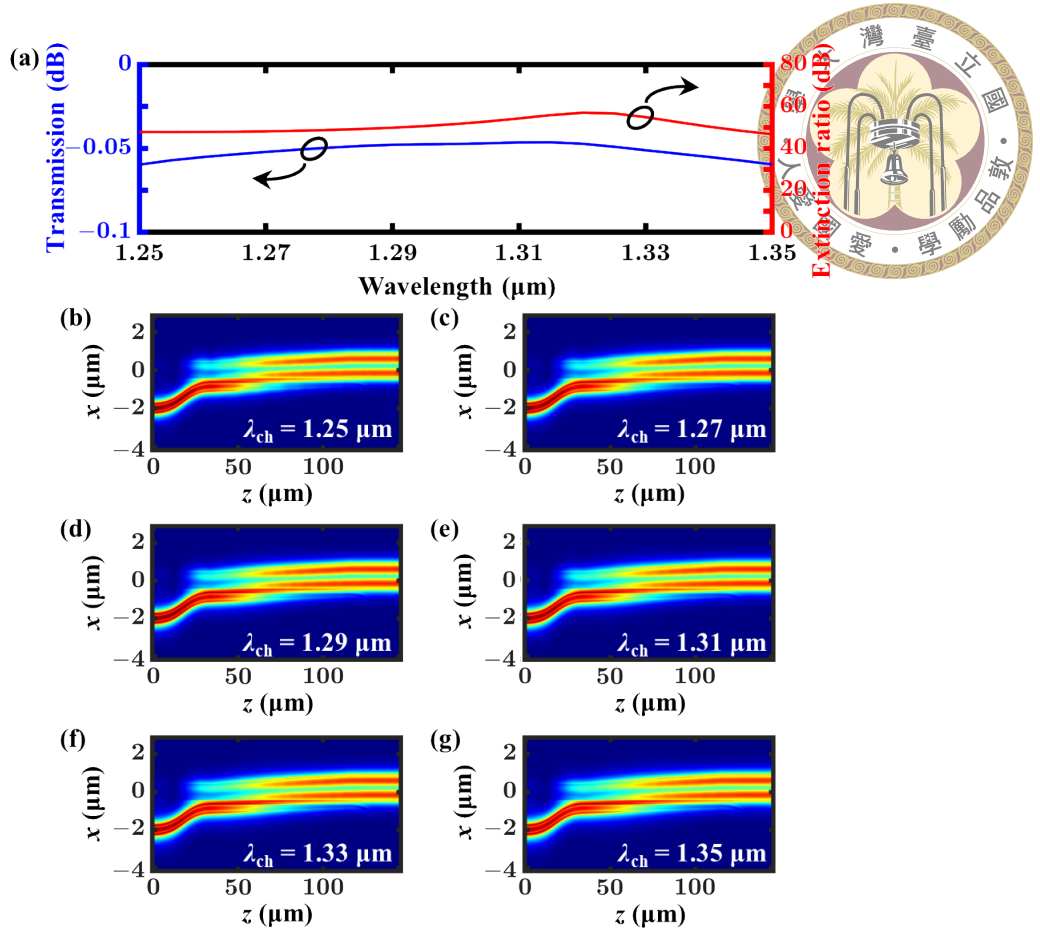


Figure 4.6: (a) Simulated transmission (blue) of the TE_0 mode at cross port, and extinction ratio (red) between the dropped TE_0 and remaining TE_1 modes. (b)–(g) Electric-field profiles at six wavelengths.

a proper order, with each group formed by the same BADC followed by the MMWBG designed for the desired channel. Regarding the cascading order, the MMWBG designed for the shorter channel wavelength is cascaded with higher priority to conduct the contra-directional coupling when demultiplexing, given that the MMWBGs designed for longer channel wavelengths would compromise the forward TE_0 -mode transmission at shorter wavelengths by approximately 1–2 dB, as shown in Fig. 4.4(b). Fig. 4.7 illustrates the schematic configuration of the overall O-band CWDM filter as well as its simulated filtering responses. The simulation results show that the flat-top responses with low ELs below 1 dB (0.17/0.3/0.4/0.6 dB at 1.27/1.29/1.31/1.33 μm), a high channels uniformity above −0.45 dB, a broad $\text{BW}_{1-\text{dB}} \sim 13.45$ nm, an ultra-low channel XT of −28 dB, ultra-broad $\text{ABW}_{28-\text{dB}}$ and $\text{ABW}_{20-\text{dB}}$ of approximately 14.35 and 15.7 nm, respectively, are

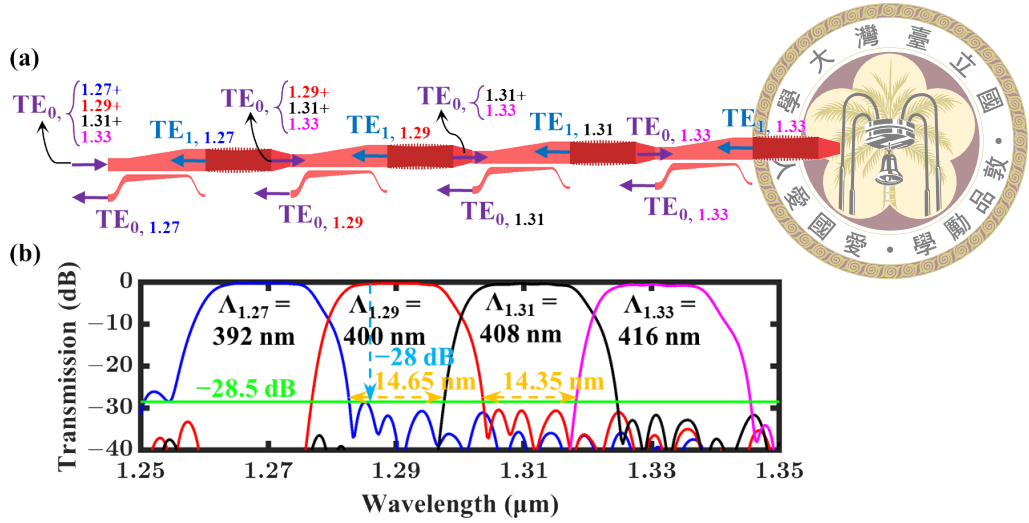


Figure 4.7: (a) Schematic configuration of the proposed overall O-band CWDM filter and (b) its simulated filtering responses.

obtained. Table 4.3 shows performance comparison, indicating the ultra-low channel XT of -28 dB with its ultra-broad available bandwidth ~ 14.35 nm, outperforming all other CWDM filters in the literature.

4.2 Analysis of fabrication tolerance

As mentioned earlier in the former section, only the tolerance of the proposed MMWBG to fabrication errors is analyzed to evaluate the overall device robustness, under the reasonable assumption of the high tolerance for the BADC. To ensure that a sufficient degree of robustness would be demonstrated, a value that is three times the standard error during manufacture is selected for the analysis. Given a standard error of 6 nm provided by a representative foundry service, an over-etching error W_e within ± 18 nm with a step of 6 nm is used to evaluate the tolerance. For each tolerance analysis, the patterned core region is considered as an island, with the outermost region (width and length) decreased/increased by the fabrication error. The concept is utilized so that both the corrugated width and duty cycle of the WBG are adjusted in terms of W_e . Figure 4.8 shows the filtering responses of the proposed MMWBGs at four channels in terms of the different over-etching errors. The

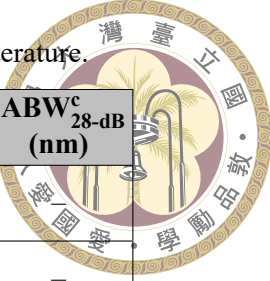


Table 4.3: Performance comparison of CWDM filters in the literature.

Structure	EL (dB)	XT (dB)	Mat./ Band	BW ^a _{1-dB} (nm)	ABW ^b _{20-dB} (nm)	ABW ^c _{28-dB} (nm)
AWG [48] (Fig. 6(a))	5–6	−27	InP/ O	3	< 3	—
AWG [10] (Fig. 14)	~3	−25	Si/ O	~11	~12.8	—
EG ^d [106] (Fig. 5(d))	~3	−22	Si/ C	~5.7	~7.5	—
EG [37] (Fig. 3(c))	2–3	−30	SiN/ O	~6.7	5.7	< 3
MMI ^e [35] (Fig. 3(d))	2–3	−13	Si/ C	8.5	—	—
MMI [34] (Fig. 6(b))	< 1	−18	LN/ O	7.5	—	—
MZI [58] (Fig. 6(b))	~0.5	−16	Si/ C	~14	—	—
MZI [52] (Fig. 5(d))	< 1	−23	Si/ O	18	~3.7	—
MZI [60] (Fig. 3(b))	1.78	−15	SiN/ O	11.86	—	—
WBG ^f [45] (Fig. 6(b))	~1	−12	Si/ C	12	—	—
WBG [40] (Fig. 7)	< 1	−13	Si/ C	7	—	—
WBG [41] (Fig. 5(c))	~1	−20	Si/ O	15	~12	—
WBG [42] (Fig. 5(b))	< 1.1	−18	LN/ C	10	—	—
Proposed Structure	< 1	−28	SiN/ O	13.45	~15.7	14.35

^a 1-dB bandwidth measured from the transmission peak.

^b Available bandwidth for channel XT below −20 dB, *i.e.*, ABW_{20-dB}.

^c Available bandwidth for channel XT below −28 dB, *i.e.*, ABW_{28-dB}.

^d Echelle grating; ^e Multi-mode interferometer; ^f Waveguide Bragg grating.

corresponding resonant wavelengths is as expected, appearing blue-shifted (red-shifted) due to the decreased (increased) effective indices of both the TE₀ and TE₁ modes owing to the over-etching errors $W_e > 0$ ($W_e < 0$). The XTs given in Fig. 4.8 remain below −24.2 dB even in the case of three times the standard error, *i.e.*, ±18 nm, demonstrating the high tolerance to fabrication error of the proposed device for the O-band CWDM system. The resulting high fabrication tolerance can be attributed to three advantageous

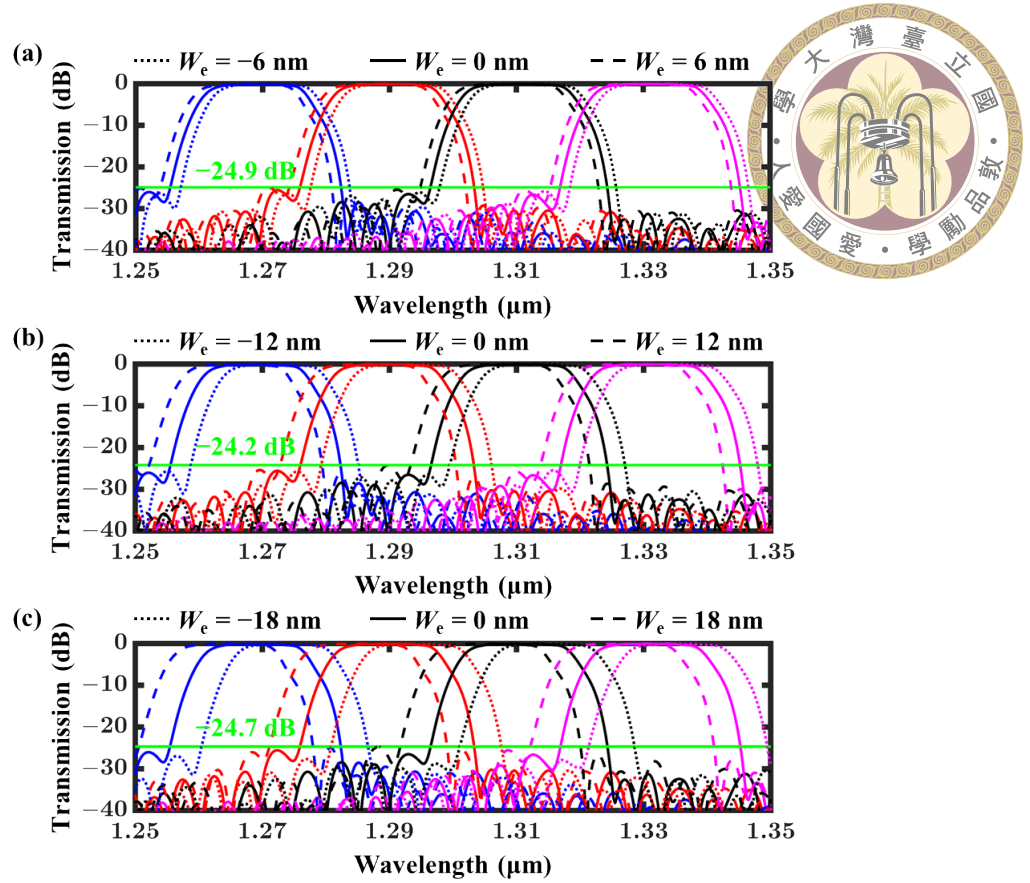


Figure 4.8: Simulated filtering responses of the individual MMWBGs using 3-D FDTD method at the four channels in terms of the configuration in Fig. 4.1 and the given over-etching errors W_e within (± 18 nm) with a step of 6 nm.

conditions: (i) low index contrast brought by the utilized silicon-nitride layer, (ii) a wide core width allowing for guiding the TE_1 mode but at the small effective indices at four channels, (iii) the coarse channel spacing of 20 nm configured for the CWDM systems. To ensure the filter is entirely considered, simulated filtering responses of the overall CWDM filter at the different over-etching errors W_e are conducted using the compact model based on the S-parameter concept, as shown in Fig. 4.9. The simulation results indicate the impact of the deviated MMWBGs on the performances of the overall CWDM filter, illustrating the flat-top responses offering a low EL below 1 dB and an ultra-low XT below -25 dB even for the extreme cases with $W_e = \pm 18$ nm, showing the great potential and high attractiveness of the device for use in the O-band CWDM systems.

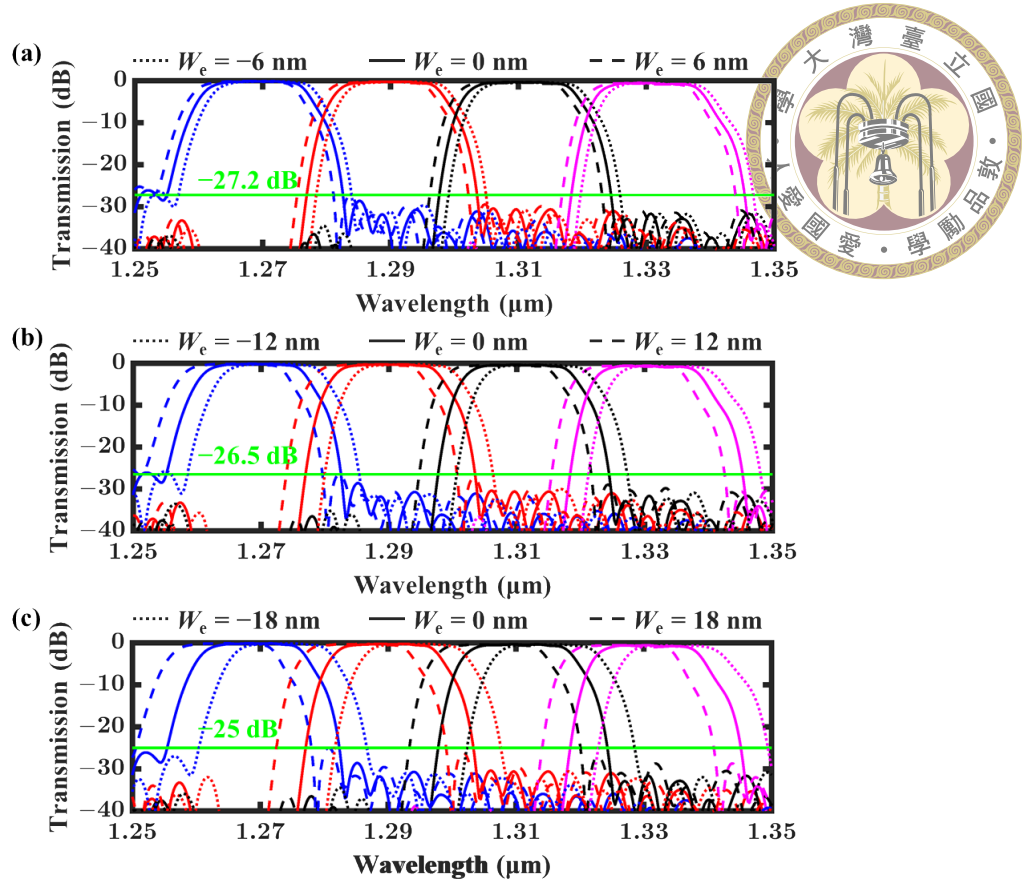
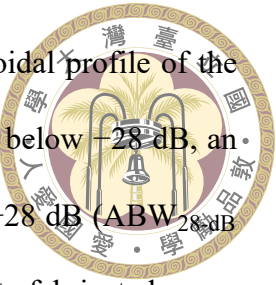


Figure 4.9: Simulated filtering responses of the overall CWDM filter using 3-D FDTD method followed by cascaded S-parameter calculation at the four channels in terms of the configuration in Fig. 4.7 and the given over-etching errors W_e .

4.3 Summary

A wavelength division (de)multiplexing (WDM) filter with ultra-low channel crosstalk (XT) and high fabrication tolerance was achieved using multi-mode waveguide Bragg grating (MMWBG). The device was based on a silicon-nitride layer over a silicon-on-insulator to achieve the critical dimension of ≥ 150 nm to permit future fabrication at a SiPh foundry service. By introducing an appropriate and balanced width corrugation, *i.e.*, the same positive and negative width change referenced to the unperturbed width, into the amplitude apodization, the dc-shift term of the permittivity perturbation was eliminated to allow for efficient design of the required Bragg period, so that the period can be evaluated by simply using channel wavelengths and guided-mode effective indices. For

lower XTs, phase apodization was also employed to achieve a sinusoidal profile of the coupling ac term. The results indicated that an ultra-low channel XT below -28 dB, an ultra-broad available bandwidth of 14.35 nm for channel XT below -28 dB ($ABW_{28\text{-dB}} \sim 14.35$ nm), an ultra-broad $ABW_{20\text{-dB}} \sim 15.7$ nm, and a high tolerance to fabricated errors within (± 18 nm) were achieved, showing the great potential and high attractiveness of the proposed MMWBGs for use in the O-band CWDM telecommunication systems.





Chapter 5 Conclusion

5.1 Summary

In this dissertation, two approaches to addressing the issue of the wavelength misalignment among the desired channel wavelengths, the channel filtering wavelengths, and the optical lasing wavelengths were presented for the O-band CWDM systems. The first one was implemented with a thermally bi-directionally tunable AWG (TBDTAWG) (Chapter 3), while the other one was with the Bragg grating-assisted contra-directional coupler (Chapter 4).

In Chapter 3, the TBDTAWG was proposed and implemented on the Silicon Photonics (SiPh) service provided by the representative foundry, *i.e.*, Interuniversity Microelectronics Centre. By utilizing the complementary phase contributions in the S-shaped architecture, a thermally bi-directionally tunable function was achieved despite using only materials with positive thermo-optic coefficients of silicon and silicon dioxide. Moreover, a parallel-circuit configuration for the on-chip heaters was utilized to significantly reduce the required voltages for tuning. Given the ultra-low footprint and high thermal conductivity of the single-mode silicon waveguide, the required thermal power for tuning was significantly reduced. From the measurement results, a thermally bi-directionally tunable feasibility was demonstrated without compromising the excess loss (EL) and crosstalk (XT). The measured tuning efficiency of ± 30.5 nm/W with wide tuning range ~ 8 nm at



ultra-low voltage of 2.5 V outperformed the other tunable AWGs to the best of the authors' knowledge, showing the potential of the device for both coarse (CWDM) and dense WDM (DWDM) systems.

In Chapter 4, on the other hand, the wavelength misalignment issue was addressed using the Bragg grating-assisted contra-directional coupler. By utilizing a properly designed amplitude apodization, *i.e.*, an appropriate width corrugations, at both waveguide side walls of the device, the multi-mode waveguide Bragg grating (MMWBG) structures can be efficiently designed based on the perturbed-permittivity coupled mode theory. To relax the critical dimension of required Bragg period for the O-band operation, silicon-nitride layer, instead of silicon one, with lower index was utilized. In addition, a phase apodization was introduced by shifting one of both side-wall corrugations to realize the TE₀–TE₁ mode contra-directionally coupling. The simulation results the four individual MMWBGs showed that an ultra-low crosstalk below –25.5 dB, an ultra-broad available bandwidth of 13.5 nm for channel crosstalk below –25 dB (ABW_{25-dB} ~13.5 nm), and an ultra-high fabrication tolerance of ±18 nm were achieved. Furthermore, the simulation results of the overall O-band CWDM filter indicated that an ultra-low channel XT below –28 dB, an ultra-broad available bandwidth of 14.35 nm for channel XT below –28 dB (ABW_{28-dB} ~14.35 nm), an ultra-broad ABW_{20-dB} ~15.7 nm, and a high tolerance to fabricated errors within ±18 nm were achieved. Compared to other CWDM filters in the literature, the proposed device in this study has the broadest ABW_{28-dB} of 14.35 nm, showing the great potential and high attractiveness for use in the CWDM telecommunication systems.

In summary, both devices are attractive owing to their special features. For the DWDM system with a demand for a small footprint, the demonstrated TBDTAWG is

a good choice to achieve multiple-channel and low-crosstalk purpose. On the other hand, for the CWDM system with a requirement for ultra-low XT, broad ABW_{28-dB}, and high-fabrication tolerance, the proposed CWDM filter using MMWBGs is a proper choice.



5.2 Suggestion for future work

For the TBDTAWG, the EL and XT can be improved with more precise control of the incremental phase distributions or a larger array number N_a in the passive design, however, at the cost of larger required number of heaters in the active design. Moreover, both them can also be further reduced by utilizing a silicon-nitride layer as the core material for lower index contrast. Given the tapered waveguides at the interfaces between FPRs and arrayed waveguides were realized with the wider width W_t of 1.7 μm , an induced higher-order mode at the coupling regions of arrayed waveguides might lead to optical loss as well as inaccurate phase distributions. To address this, a single-mode core width W_t must be chosen at the interfaces between FPRs and arrayed waveguides, as mentioned in Section 3.4. In addition to the width, the additional shallowed-etched region must be implemented with a designed length so that the mode coupling between arrayed waveguides could be suppressed when entering into the phase control region.

For the MMWBG, although the XT and SLI can be reduced with appropriate width corrugations based on silicon-nitride layer, the worst SLI of 6.66 dB was obtained at Channel 1.33. This can be attributed to the different local averaged effective indices along the propagation direction due to the introduction of the phase apodization, leading to the unwanted dc-shift term of the coupling coefficient. To compensate that, the duty cycle can be included as an additional degree of freedom for optimization, however, at the cost of other degraded performances.

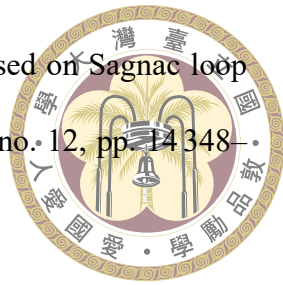


References

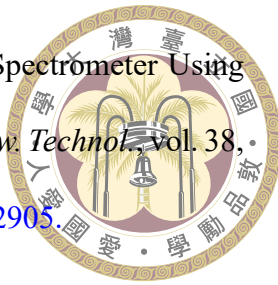
- [1] R. Kashyap, “Theory of Fiber Bragg Gratings,” in *Fiber Bragg Gratings*, 2nd ed., R. Kashyap, Ed. Academic Press, 2010, ch. 4, pp. 119–187. ISBN 978-0-12-372579-0 doi: [10.1016/B978-0-12-372579-0.00004-1](https://doi.org/10.1016/B978-0-12-372579-0.00004-1).
- [2] M. Smit and C. Van Dam, “PHASAR-based WDM-devices: Principles, design and applications,” *IEEE J. Sel. Topics Quantum Electron.*, vol. 2, no. 2, pp. 236–250, June 1996, doi: [10.1109/2944.577370](https://doi.org/10.1109/2944.577370).
- [3] M. Smit, “New focusing and dispersive planar component based on an optical phased array,” *Electron. Lett.*, vol. 24, no. 7, pp. 385–386, Mar. 1988, doi: [10.1049/el:19880260](https://doi.org/10.1049/el:19880260).
- [4] M. Amersfoort *et al.*, “Passband broadening of integrated arrayed waveguide filters using multimode interference couplers,” *Electron. Lett.*, vol. 32, no. 5, pp. 449–451, Feb. 1996, doi: [10.1049/el:19960344](https://doi.org/10.1049/el:19960344).
- [5] P. M. noz *et al.*, “Analysis and design of arrayed waveguide gratings with MMI couplers,” *Opt. Exp.*, vol. 9, no. 7, pp. 328–338, Sep. 2001, doi: [10.1364/OE.9.000328](https://doi.org/10.1364/OE.9.000328).
- [6] J. Soole *et al.*, “Use of multimode interference couplers to broaden the passband of wavelength-dispersive integrated WDM filters,” *IEEE Photon. Technol. Lett.*, vol. 8, no. 10, pp. 1340–1342, Oct. 1996, doi: [10.1109/68.536648](https://doi.org/10.1109/68.536648).



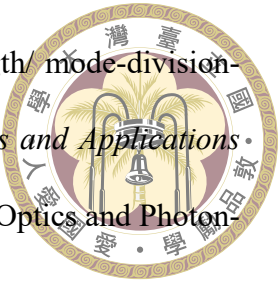
- [7] S. Pathak *et al.*, “Optimized Silicon AWG With Flattened Spectral Response Using an MMI Aperture,” *J. Lightw. Technol.*, vol. 31, no. 1, pp. 87–93, Jan. 2013, doi: [10.1109/JLT.2012.2231399](https://doi.org/10.1109/JLT.2012.2231399).
- [8] S. Pathak *et al.*, “Compact SOI-based AWG with flattened spectral response using a MMI,” in *8th IEEE International Conference on Group IV Photonics*, Sep. 2011, Conference Proceedings, pp. 45–47. ISBN 1949-209X doi: [10.1109/GROUP4.2011.6053710](https://doi.org/10.1109/GROUP4.2011.6053710).
- [9] J.-H. Jung, “Optimization for Arrayed Waveguide Grating having MMI Coupler for Flattened Transfer Function,” *J. Opt. Soc. Korea*, vol. 10, no. 4, pp. 169–173, Dec. 2006.
- [10] Y. Zheng *et al.*, “Design of 4-channel AWG Multiplexer/demultiplexer for CWDM system,” *Optik*, vol. 201, p. 163513, Jan. 2020, doi: [10.1016/j.ijleo.2019.163513](https://doi.org/10.1016/j.ijleo.2019.163513).
- [11] K. Okamoto and A. Sugita, “Flat spectral response arrayed-waveguide grating multiplexer with parabolic waveguide horns,” *Electron. Lett.*, vol. 32, no. 18, pp. 1661–1662, Aug. 1996, doi: [10.1049/el:19961108](https://doi.org/10.1049/el:19961108).
- [12] C. Henry *et al.*, “Glass waveguides on silicon for hybrid optical packaging,” *J. Lightw. Technol.*, vol. 7, no. 10, pp. 1530–1539, Oct. 1989, doi: [10.1109/50.39094](https://doi.org/10.1109/50.39094).
- [13] Q. Lai *et al.*, “Simple technologies for fabrication of low-loss silica waveguides,” *Electron. Lett.*, vol. 28, pp. 1000–1001, May 1992, doi: [10.1049/el:19920635](https://doi.org/10.1049/el:19920635).
- [14] K. Okamoto and H. Yamada, “Arrayed-waveguide grating multiplexer with flat spectral response,” *Opt. Lett.*, vol. 20, no. 1, pp. 43–45, Jan. 1995, doi: [10.1364/OL.20.000043](https://doi.org/10.1364/OL.20.000043).



- [15] B. Gargallo *et al.*, “Reflective arrayed waveguide gratings based on Sagnac loop reflectors with custom spectral response,” *Opt. Exp.*, vol. 22, no. 12, pp. 14 348–14 362, June 2014, doi: [10.1364/OE.22.014348](https://doi.org/10.1364/OE.22.014348).
- [16] K. Okamoto and H. Yamada, “Arrayed-waveguide grating multiplexer with flat spectral response,” *Opt. Lett.*, vol. 20, no. 1, pp. 43–45, Jan. 1995, doi: [10.1364/OL.20.000043](https://doi.org/10.1364/OL.20.000043).
- [17] C. Dragone, “Efficient techniques for widening the passband of a wavelength router,” *J. Lightw. Technol.*, vol. 16, no. 10, pp. 1895–1906, Oct. 1998, doi: [10.1109/50.721078](https://doi.org/10.1109/50.721078).
- [18] K. Takada *et al.*, “Measurement of phase error distributions in silica-based arrayed-waveguide grating multiplexers by using Fourier transform spectroscopy,” *Electron. Lett.*, vol. 30, no. 20, pp. 1671–1672, Sep. 1994, doi: [10.1049/el:19941113](https://doi.org/10.1049/el:19941113).
- [19] S. Pathak *et al.*, “Compact SOI-based polarization diversity wavelength demultiplexer circuit using two symmetric AWGs,” *Opt. Exp.*, vol. 20, no. 26, pp. B493–B500, Dec. 2012, doi: [10.1364/OE.20.00B493](https://doi.org/10.1364/OE.20.00B493).
- [20] S. Pathak *et al.*, “Effect of Mask Discretization on Performance of Silicon Arrayed Waveguide Gratings,” *IEEE Photon. Technol. Lett.*, vol. 26, no. 7, pp. 718–721, Apr. 2014, doi: [10.1109/LPT.2014.2303793](https://doi.org/10.1109/LPT.2014.2303793).
- [21] J. Zou *et al.*, “Novel Wavelength Multiplexer Using $(N + 1) \times (N + 1)$ Arrayed Waveguide Grating and Polarization-Combiner-Rotator on SOI Platform,” *J. Lightw. Technol.*, vol. 39, no. 8, pp. 2431–2437, Apr. 2021, doi: [10.1109/JLT.2021.3053837](https://doi.org/10.1109/JLT.2021.3053837).



- [22] J. Zou *et al.*, “High Resolution and Ultra-Compact On-Chip Spectrometer Using Bidirectional Edge-Input Arrayed Waveguide Grating,” *J. Lightw. Technol.*, vol. 38, no. 16, pp. 4447–4453, Aug. 2020, doi: [10.1109/JLT.2020.2992905](https://doi.org/10.1109/JLT.2020.2992905).
- [23] S. Pathak *et al.*, “Design trade-offs for silicon-on-insulator-based AWGs for (de)multiplexer applications,” *Opt. Lett.*, vol. 38, no. 16, pp. 2961–2964, Aug. 2013, doi: [10.1364/OL.38.002961](https://doi.org/10.1364/OL.38.002961).
- [24] A. Malik *et al.*, “Germanium-on-Silicon Mid-Infrared Arrayed Waveguide Grating Multiplexers,” *IEEE Photon. Technol. Lett.*, vol. 25, no. 18, pp. 1805–1808, Sep. 2013, doi: [10.1109/LPT.2013.2276479](https://doi.org/10.1109/LPT.2013.2276479).
- [25] D. Martens *et al.*, “Compact Silicon Nitride Arrayed Waveguide Gratings for Very Near-Infrared Wavelengths,” *IEEE Photon. Technol. Lett.*, vol. 27, no. 2, pp. 137–140, Jan. 2015, doi: [10.1109/LPT.2014.2363298](https://doi.org/10.1109/LPT.2014.2363298).
- [26] D. Melati *et al.*, “Compact and Low Crosstalk Echelle Grating Demultiplexer on Silicon-On-Insulator Technology,” *Electronics*, vol. 8, no. 6, p. 687, June 2019, doi: [10.3390/electronics8060687](https://doi.org/10.3390/electronics8060687).
- [27] T. D. Bucio *et al.*, “Silicon Nitride Photonics for the Near-Infrared,” *IEEE J. Sel. Topics Quantum Electron.*, vol. 26, no. 2, pp. 1–13, Sep. 2020, doi: [10.1109/jstqe.2019.2934127](https://doi.org/10.1109/jstqe.2019.2934127).
- [28] D. Dai *et al.*, “Multimode silicon photonic devices,” in *Integrated Optics: Devices, Materials, and Technologies XXV*, S. M. García-Blanco and P. Cheben, Eds., vol. 11689, International Society for Optics and Photonics. SPIE, Mar. 2021, p. 116890N, doi: [10.1117/12.2577026](https://doi.org/10.1117/12.2577026).



- [29] D. Dai *et al.*, “Silicon photonic devices for wavelength/ mode-division-multiplexing,” in *Integrated Optics: Design, Devices, Systems and Applications VI*, P. Cheben *et al.*, Eds., vol. 11775, International Society for Optics and Photonics. SPIE, Apr. 2021, p. 117750E, doi: [10.1117/12.2588925](https://doi.org/10.1117/12.2588925).
- [30] J. Jiang *et al.*, “Silicon lateral-apodized add–drop filter for on-chip optical interconnection,” *Appl. Opt.*, vol. 56, no. 30, pp. 8425–8429, Oct. 2017, doi: [10.1364/AO.56.008425](https://doi.org/10.1364/AO.56.008425).
- [31] N. Saha *et al.*, “Tunable narrow band add-drop filter design based on apodized long period waveguide grating assisted co-directional coupler,” *Opt. Exp.*, vol. 30, no. 16, pp. 28 632–28 646, Aug. 2022, doi: [10.1364/OE.461876](https://doi.org/10.1364/OE.461876).
- [32] S. Kumar *et al.*, “Side-lobe reduction by cascading Bragg grating filters on a Si-photonic chip,” *Opt. Exp.*, vol. 30, no. 6, pp. 9983–9991, Mar. 2022, doi: [10.1364/OE.446588](https://doi.org/10.1364/OE.446588).
- [33] L. Liu *et al.*, “Dual Functional WDM Devices for Multiplexing and Demultiplexing on Silicon-on-Insulator,” in *The International Photonics and Optoelectronics Meeting 2017*, ser. OSA Technical Digest (online). Optical Society of America, Nov. 2017, Conference Proceedings, p. AS3A.25, doi: [10.1364/ASA.2017.AS3A.25](https://doi.org/10.1364/ASA.2017.AS3A.25).
- [34] G. Chen *et al.*, “Four-channel CWDM device on a thin-film lithium niobate platform using an angled multimode interferometer structure,” *Photonics Res.*, vol. 10, no. 1, pp. 8–13, Jan. 2022, doi: [10.1364/prj.438816](https://doi.org/10.1364/prj.438816).



- [35] Y. Hu *et al.*, “Wavelength division (de)multiplexing based on dispersive self-imaging,” *Opt. Lett.*, vol. 36, no. 23, pp. 4488–4490, Dec. 2011, doi: [10.1364/OL.36.004488](https://doi.org/10.1364/OL.36.004488).
- [36] T. D. Bucio *et al.*, “N-rich silicon nitride angled MMI for coarse wavelength division (de)multiplexing in the O-band,” *Opt. Lett.*, vol. 43, no. 6, pp. 1251–1254, Mar. 2018, doi: [10.1364/ol.43.001251](https://doi.org/10.1364/ol.43.001251).
- [37] Q. Wilmart *et al.*, “A Versatile Silicon-Silicon Nitride Photonics Platform for Enhanced Functionalities and Applications,” *Appl. Sci.*, vol. 9, no. 2, p. 255, Jan. 2019, doi: [10.3390/app9020255](https://doi.org/10.3390/app9020255).
- [38] Q. Wilmart *et al.*, “Si-SiN Photonic Platform for CWDM Applications,” in *2018 IEEE 15th International Conference on Group IV Photonics (GFP)*, Aug. 2018, Conference Proceedings, pp. 1–2. ISBN 1949-209X doi: [10.1109/GROUP4.2018.8478747](https://doi.org/10.1109/GROUP4.2018.8478747).
- [39] Y. Zheng *et al.*, “Compact low-loss low-crosstalk echelle grating demultiplexer on silicon-on-insulator for CWDM,” *Optik*, vol. 249, p. 168236, 2022, doi: [10.1016/j.ijleo.2021.168236](https://doi.org/10.1016/j.ijleo.2021.168236).
- [40] J. Chen and Y. Shi, “Flat-Top CWDM (De)Multiplexers Based on Contradirectional Couplers With Subwavelength Gratings,” *IEEE Photon. Technol. Lett.*, vol. 31, no. 24, pp. 2003–2006, Nov. 2019, doi: [10.1109/LPT.2019.2953379](https://doi.org/10.1109/LPT.2019.2953379).
- [41] D. Liu *et al.*, “Four-Channel CWDM (de)Multiplexers Using Cascaded Multimode Waveguide Gratings,” *IEEE Photon. Technol. Lett.*, vol. 32, no. 4, pp. 192–195, Feb. 2020, doi: [10.1109/LPT.2020.2966073](https://doi.org/10.1109/LPT.2020.2966073).



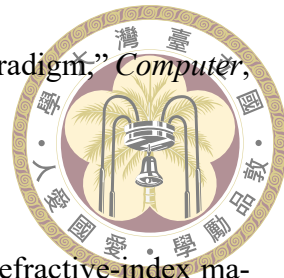
- [42] Y. Liu *et al.*, “C-band four-channel CWDM (de-)multiplexers on a thin film lithium niobate–silicon rich nitride hybrid platform,” *Opt. Lett.*, vol. 46, no. 19, pp. 4726–4729, Oct. 2021, doi: [10.1364/OL.437681](https://doi.org/10.1364/OL.437681).
- [43] Y. Zhao *et al.*, “Multi-Channel WDM (De)Multiplexer Based on Multimode Contra-Directional Coupling Using Dielectric Etches,” in *Asia Communications and Photonics Conference/International Conference on Information Photonics and Optical Communications 2020 (ACP/IPOC)*, ser. OSA Technical Digest. Optical Society of America, Oct. 2020, Conference Proceedings, p. M4A.178, doi: [10.1364/ACPC.2020.M4A.178](https://doi.org/10.1364/ACPC.2020.M4A.178).
- [44] E. Zubkova *et al.*, “CWDM demultiplexer using anti-reflection, contra-directional couplers based on silicon nitride rib waveguide,” *J. Phys. Conf. Ser.*, vol. 1410, no. 1, p. 012179, Dec. 2019, doi: [10.1088/1742-6596/1410/1/012179](https://doi.org/10.1088/1742-6596/1410/1/012179).
- [45] W. Shi *et al.*, “Ultra-compact, flat-top demultiplexer using anti-reflection contra-directional couplers for CWDM networks on silicon,” *Opt. Exp.*, vol. 21, no. 6, pp. 6733–6738, Mar. 2013, doi: [10.1364/OE.21.006733](https://doi.org/10.1364/OE.21.006733).
- [46] S. Cheung and M. R. T. Tan, “Ultra-low loss and fabrication tolerant silicon nitride (Si_3N_4) (de-)muxes for 1- μm CWDM optical interconnects,” in *Optical Fiber Communication Conference (OFC) 2020*. Optica Publishing Group, 2020, p. M3F.6, doi: [10.1364/OFC.2020.M3F.6](https://doi.org/10.1364/OFC.2020.M3F.6).
- [47] S. S. Cheung and M. R. T. Tan, “Silicon Nitride (Si_3N_4) (De-)Multiplexers for 1- μm CWDM Optical Interconnects,” *J. Lightw. Technol.*, vol. 38, no. 13, pp. 3404–3413, Nov. 2020, doi: [10.1364/JLT.38.003404](https://doi.org/10.1364/JLT.38.003404).



- [48] P. Pan *et al.*, “Compact 4-channel AWGs for CWDM and LAN WDM in data center monolithic applications,” *Opt. Laser Technol.*, vol. 75, pp. 177–181, Dec. 2015, doi: [10.1016/j.optlastec.2015.07.005](https://doi.org/10.1016/j.optlastec.2015.07.005).
- [49] S. Guerber *et al.*, “Design and integration of an O-band silicon nitride AWG for CWDM applications,” in *2017 IEEE 14th International Conference on Group IV Photonics (GFP)*, Aug. 2017, pp. 133–134. ISSN 1949-209X doi: [10.1109/GROUP4.2017.8082232](https://doi.org/10.1109/GROUP4.2017.8082232).
- [50] S. Guerber *et al.*, “Polarization independent and temperature tolerant AWG based on a silicon nitride platform,” *Opt. Lett.*, vol. 45, no. 23, p. 6559, Dec. 2020, doi: [10.1364/ol.411332](https://doi.org/10.1364/ol.411332).
- [51] C. R. Doerr *et al.*, “Eight-Channel SiO₂/Si₃N₄/Si/Ge CWDM Receiver,” *IEEE Photon. Technol. Lett.*, vol. 23, no. 17, pp. 1201–1203, Sep. 2011, doi: [10.1109/LPT.2011.2158091](https://doi.org/10.1109/LPT.2011.2158091).
- [52] H. Xu and Y. Shi, “Flat-Top CWDM (De)Multiplexer Based on MZI With Bent Directional Couplers,” *IEEE Photon. Technol. Lett.*, vol. 30, no. 2, pp. 169–172, Jan. 2018, doi: [10.1109/LPT.2017.2779489](https://doi.org/10.1109/LPT.2017.2779489).
- [53] H. Xu *et al.*, “Low-crosstalk and fabrication-tolerant four-channel CWDM filter based on dispersion-engineered Mach-Zehnder interferometers,” *Opt. Exp.*, vol. 29, no. 13, pp. 20 617–20 631, June 2021, doi: [10.1364/oe.428352](https://doi.org/10.1364/oe.428352).
- [54] J. Y. Lee *et al.*, “Fabrication-Tolerant Nitride Lattice Filter for CWDM,” in *Optical Fiber Communication Conference (OFC) 2021*, ser. OSA Technical Digest, P. K. J. X. C. C. R. C. C. Dong and M. Li, Eds. Optical Society of America, Jan. 2021, Conference Proceedings, p. Tu5B.2, doi: [10.1364/OFC.2021.Tu5B.2](https://doi.org/10.1364/OFC.2021.Tu5B.2).



- [55] T. H. Yen and Y. J. Hung, “Fabrication-Tolerant CWDM (de)Multiplexer Based on Cascaded Mach-Zehnder Interferometers on Silicon-on-Insulator,” *J. Lightw. Technol.*, vol. 39, no. 1, pp. 146–153, Jan. 2021, doi: [10.1109/JLT.2020.3026314](https://doi.org/10.1109/JLT.2020.3026314).
- [56] J. C. Mikkelsen *et al.*, “Polarization-insensitive silicon nitride Mach-Zehnder lattice wavelength demultiplexers for CWDM in the O-band,” *Opt. Exp.*, vol. 26, no. 23, pp. 30 076–30 084, Nov. 2018, doi: [10.1364/oe.26.030076](https://doi.org/10.1364/oe.26.030076).
- [57] H. Xu *et al.*, “Polarization-insensitive four-channel coarse wavelength-division (de)multiplexer based on Mach-Zehnder interferometers with bent directional couplers and polarization rotators,” *Opt. Lett.*, vol. 43, no. 7, pp. 1483–1486, Apr. 2018, doi: [10.1364/OL.43.001483](https://doi.org/10.1364/OL.43.001483).
- [58] X. Jiang *et al.*, “Compact CWDM interleaver based on an interfering loop containing a one-dimensional Fabry-Perot cavity,” *Opt. Lett.*, vol. 43, no. 5, pp. 1071–1074, Mar. 2018, doi: [10.1364/OL.43.001071](https://doi.org/10.1364/OL.43.001071).
- [59] J. R. Ong *et al.*, “Wafer-Level Characterization of Silicon Nitride CWDM (De)Multiplexers Using Bayesian Inference,” *IEEE Photon. Technol. Lett.*, vol. 32, no. 15, pp. 917–920, Aug. 2020, doi: [10.1109/LPT.2020.3004850](https://doi.org/10.1109/LPT.2020.3004850).
- [60] G. Gao *et al.*, “Silicon nitride O-band (de)multiplexers with low thermal sensitivity,” *Opt. Exp.*, vol. 25, no. 11, p. 12260, May 2017, doi: [10.1364/oe.25.012260](https://doi.org/10.1364/oe.25.012260).
- [61] D. Liu *et al.*, “Silicon photonic filters,” *Microw. and Opt. Technol. Lett.*, vol. 63, no. 9, pp. 2252–2268, July 2020, doi: [10.1002/mop.32509](https://doi.org/10.1002/mop.32509).
- [62] T. Baehr-Jones *et al.*, “Myths and rumours of silicon photonics,” *Nature Photon.*, vol. 6, no. 4, pp. 206–208, Mar. 2012, doi: [10.1038/nphoton.2012.66](https://doi.org/10.1038/nphoton.2012.66).



- [63] L. Benini and G. D. Micheli, “Networks on chips: a new SoC paradigm,” *Computer*, vol. 35, no. 1, pp. 70–78, Jan. 2002, doi: [10.1109/2.976921](https://doi.org/10.1109/2.976921).
- [64] Z. Wang *et al.*, “Compact silicon three-mode multiplexer by refractive-index manipulation on a multi-mode interferometer,” *Opt. Exp.*, vol. 29, no. 9, pp. 13 899–13 907, Apr. 2021, doi: [10.1364/OE.423973](https://doi.org/10.1364/OE.423973).
- [65] L. Chrostowski *et al.*, “Silicon photonic resonator sensors and devices,” in *Laser Resonators, Microresonators, and Beam Control XIV*, A. V. Kudryashov *et al.*, Eds., vol. 8236, International Society for Optics and Photonics. SPIE, Feb. 2012, p. 823620, doi: [10.1117/12.916860](https://doi.org/10.1117/12.916860).
- [66] D. Dai, “Advanced Passive Silicon Photonic Devices With Asymmetric Waveguide Structures,” *Proc. IEEE*, vol. 106, no. 12, pp. 2117–2143, May 2018, doi: [10.1109/JPROC.2018.2822787](https://doi.org/10.1109/JPROC.2018.2822787).
- [67] D. Dai *et al.*, “10-Channel Mode (de)multiplexer with Dual Polarizations,” *Laser Photon. Rev.*, vol. 12, no. 1, p. 1700109, Jan. 2018, doi: [10.1002/lpor.201700109](https://doi.org/10.1002/lpor.201700109).
- [68] M. Ma *et al.*, “Sub-wavelength grating-assisted polarization splitter-rotators for silicon-on-insulator platforms,” *Opt. Exp.*, vol. 27, no. 13, pp. 17 581–17 591, June 2019, doi: [10.1364/OE.27.017581](https://doi.org/10.1364/OE.27.017581).
- [69] G. B. d. Farias *et al.*, “Demonstration of a low-loss and broadband Polarization Splitter-Rotator with a Polysilicon waveguide in SOI platform,” in *2019 SBFoton International Optics and Photonics Conference (SBFoton IOPC)*, Oct. 2019, Conference Proceedings, pp. 1–5, doi: [10.1109/SBFoton-IOPC.2019.8910218](https://doi.org/10.1109/SBFoton-IOPC.2019.8910218).



- [70] W. Lee *et al.*, “Coherent terahertz wireless communication using dual-parallel MZM-based silicon photonic integrated circuits,” *Opt. Exp.*, vol. 30, no. 2, pp. 2547–2563, Jan. 2022, doi: [10.1364/OE.446516](https://doi.org/10.1364/OE.446516).
- [71] N.-N. Feng *et al.*, “High speed carrier-depletion modulators with 1.4V·cm VπL integrated on 0.25 μ m silicon-on-insulator waveguides,” *Opt. Exp.*, vol. 18, no. 8, pp. 7994–7999, Apr. 2010, doi: [10.1364/OE.18.007994](https://doi.org/10.1364/OE.18.007994).
- [72] P. Fu *et al.*, “Optimization for Ultrabroadband Polarization Beam Splitters Using a Genetic Algorithm,” *IEEE Photon. J.*, vol. 11, no. 1, pp. 1–11, Feb. 2019, doi: [10.1109/JPHOT.2018.2887096](https://doi.org/10.1109/JPHOT.2018.2887096).
- [73] P.-H. Fu *et al.*, “Broadband optical waveguide couplers with arbitrary coupling ratios designed using a genetic algorithm,” *Opt. Exp.*, vol. 24, no. 26, pp. 30 547–30 561, Dec. 2016, doi: [10.1364/OE.24.030547](https://doi.org/10.1364/OE.24.030547).
- [74] C. Ye and D. Dai, “Ultra-Compact Broadband 2 × 2 3 dB Power Splitter Using a Subwavelength-Grating-Assisted Asymmetric Directional Coupler,” *J. Lightw. Technol.*, vol. 38, no. 8, pp. 2370–2375, Apr. 2020, doi: [10.1109/jlt.2020.2973663](https://doi.org/10.1109/jlt.2020.2973663).
- [75] J. Wang *et al.*, “Novel ultra-broadband polarization splitter-rotator based on mode-evolution tapers and a mode-sorting asymmetric Y-junction,” *Opt. Exp.*, vol. 22, no. 11, pp. 13 565–13 571, June 2014, doi: [10.1364/OE.22.013565](https://doi.org/10.1364/OE.22.013565).
- [76] H. Guan *et al.*, “CMOS-compatible highly efficient polarization splitter and rotator based on a double-etched directional coupler,” *Opt. Exp.*, vol. 22, no. 3, pp. 2489–2496, Feb. 2014, doi: [10.1364/OE.22.002489](https://doi.org/10.1364/OE.22.002489).



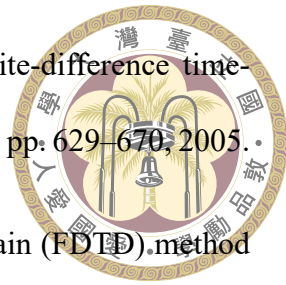
- [77] H. Guan *et al.*, "High-Efficiency Biwavelength Polarization Splitter-Rotator on the SOI Platform," *IEEE Photon. Technol. Lett.*, vol. 27, no. 5, pp. 518–521, Mar. 2015, doi: [10.1109/LPT.2014.2384451](https://doi.org/10.1109/LPT.2014.2384451).
- [78] X. Wang *et al.*, "Precise control of the coupling coefficient through destructive interference in silicon waveguide Bragg gratings," *Opt. Lett.*, vol. 39, no. 19, pp. 5519–5522, Oct. 2014, doi: [10.1364/OL.39.005519](https://doi.org/10.1364/OL.39.005519).
- [79] X. Guan *et al.*, "Low-loss ultracompact transverse-magnetic-pass polarizer with a silicon subwavelength grating waveguide," *Opt. Lett.*, vol. 39, no. 15, pp. 4514–4517, Aug. 2014, doi: [10.1364/OL.39.004514](https://doi.org/10.1364/OL.39.004514).
- [80] Y. C. Tu *et al.*, "High-Efficiency Ultra-Broadband Multi-Tip Edge Couplers for Integration of Distributed Feedback Laser With Silicon-on-Insulator Waveguide," *IEEE Photon. J.*, vol. 11, no. 4, pp. 1–13, June 2019, doi: [10.1109/JPHOT.2019.2924477](https://doi.org/10.1109/JPHOT.2019.2924477).
- [81] W. Liu *et al.*, "High Efficiency Silicon Edge Coupler Based On Uniform Arrayed Waveguides With Un-Patterned Cladding," *IEEE Photon. Technol. Lett.*, vol. 32, no. 17, pp. 1077–1080, Sep. 2020, doi: [10.1109/LPT.2020.3011188](https://doi.org/10.1109/LPT.2020.3011188).
- [82] B. Chen *et al.*, "Two-dimensional grating coupler on silicon with a high coupling efficiency and a low polarization-dependent loss," *Opt. Exp.*, vol. 28, no. 3, pp. 4001–4009, Feb. 2020, doi: [10.1364/OE.380338](https://doi.org/10.1364/OE.380338).
- [83] Y. Liu *et al.*, "Thermo-Optic Tunable Silicon Arrayed Waveguide Grating at 2- μm Wavelength Band," *IEEE Photon. J.*, vol. 12, no. 4, pp. 1–8, Aug. 2020, doi: [10.1109/JPHOT.2020.3001595](https://doi.org/10.1109/JPHOT.2020.3001595).



- [84] Y. Yang *et al.*, “Thermo-Optically Tunable Silicon AWG With Above 600 GHz Channel Tunability,” *IEEE Photon. Technol. Lett.*, vol. 27, no. 22, pp. 2351–2354, Nov. 2015, doi: [10.1109/LPT.2015.2464073](https://doi.org/10.1109/LPT.2015.2464073).
- [85] J. Zou *et al.*, “Performance improvement for silicon-based arrayed waveguide grating router,” *Opt. Exp.*, vol. 25, no. 9, pp. 9963–9973, May 2017, doi: [10.1364/OE.25.009963](https://doi.org/10.1364/OE.25.009963).
- [86] M. Lelit *et al.*, “Passive Photonic Integrated Circuits Elements Fabricated on a Silicon Nitride Platform,” *Materials*, vol. 15, no. 4, p. 1398, Feb. 2022, doi: [10.3390/ma15041398](https://doi.org/10.3390/ma15041398).
- [87] X. J. M. Leijtens *et al.*, “Arrayed Waveguide Gratings,” in *Wavelength Filters in Fibre Optics*, H. Venghaus, Ed. Berlin, Heidelberg: Springer Berlin Heidelberg, Apr. 2006, pp. 125–187. ISBN 978-3-540-31770-8 doi: [10.1007/3-540-31770-8_5](https://doi.org/10.1007/3-540-31770-8_5).
- [88] K. Okamoto, “Planar Lightwave Circuits,” in *Fundamentals of Optical Waveguides*, 3rd ed., K. Okamoto, Ed. Academic Press, 2022, ch. 9, pp. 427–684. ISBN 978-0-12-815601-8 doi: [10.1016/B978-0-12-815601-8.50009-4](https://doi.org/10.1016/B978-0-12-815601-8.50009-4).
- [89] M. Kohtoku *et al.*, “Packaged polarization-insensitive WDM monitor with low loss (7.3 dB) and wide tuning range (4.5 nm),” *IEEE Photon. Technol. Lett.*, vol. 10, no. 11, pp. 1614–1616, Nov. 1998, doi: [10.1109/68.726767](https://doi.org/10.1109/68.726767).
- [90] S. Toyoda *et al.*, “Polarization-independent low-crosstalk polymeric AWG-based tunable filter operating around 1.55 μm,” *IEEE Photon. Technol. Lett.*, vol. 11, no. 9, pp. 1141–1143, Sep. 1999, doi: [10.1109/68.784229](https://doi.org/10.1109/68.784229).
- [91] H.-m. Zhang *et al.*, “Thermo-optically tunable arrayed-waveguide-grating made of polymer/Si,” *Optoelectron. Lett.*, vol. 2, no. 4, pp. 243–245, 2006.



- [92] J. Dieckroger *et al.*, “Thermooptically tunable optical phased array in SiQ₂-Si,” *IEEE Photon. Technol. Lett.*, vol. 11, no. 2, pp. 248–250, Feb. 1999, doi: [10.1109/68.740719](https://doi.org/10.1109/68.740719).
- [93] C. Husko *et al.*, “Phase-shifted Bragg gratings in a foundry silicon nitride platform,” *OSA Continuum*, vol. 4, no. 3, pp. 933–939, Mar. 2021, doi: [10.1364/OSAC.413672](https://doi.org/10.1364/OSAC.413672).
- [94] P. S. Cross and H. Kogelnik, “Sidelobe suppression in corrugated-waveguide filters,” *Opt. Lett.*, vol. 1, no. 1, pp. 43–45, July 1977, doi: [10.1364/OL.1.000043](https://doi.org/10.1364/OL.1.000043).
- [95] D. C. Flanders *et al.*, “Grating filters for thin-film optical waveguides,” *Appl. Phys. Lett.*, vol. 24, no. 4, pp. 194–196, Nov. 1974, doi: [10.1063/1.1655150](https://doi.org/10.1063/1.1655150).
- [96] K. Okamoto, “Beam Propagation Method,” in *Fundamentals of Optical Waveguides*, 3rd ed., K. Okamoto, Ed. Academic Press, 2022, ch. 7, pp. 339–407. ISBN 978-0-12-815601-8 doi: [10.1016/B978-0-12-815601-8.50007-0](https://doi.org/10.1016/B978-0-12-815601-8.50007-0).
- [97] L. Inc., “MODE – Finite Difference Eigenmode (FDE) solver introduction.” [Online]. Available: <https://optics.ansys.com/hc/en-us/articles/360034917233-MODE-Finite-Difference-Eigenmode-FDE-solver-introduction> (Accessed Aug. 2022).
- [98] Z. Zhu and T. G. Brown, “Full-vectorial finite-difference analysis of microstructured optical fibers,” *Opt. Exp.*, vol. 10, no. 17, pp. 853–864, Aug. 2002, doi: [10.1364/OE.10.000853](https://doi.org/10.1364/OE.10.000853).
- [99] D. M. Sullivan, “Three-Dimensional Simulation,” in *Electromagnetic Simulation Using the FDTD Method*. John Wiley & Sons, Ltd, May 2013, ch. 4, pp. 85–111. ISBN 9781118646700 doi: [10.1002/9781118646700.ch4](https://doi.org/10.1002/9781118646700.ch4).



- [100] A. Taflove *et al.*, “Computational electromagnetics: the finite-difference time-domain method,” *The Electrical Engineering Handbook*, vol. 3, pp. 629–670, 2005.
- [101] S. D. Gedney, “Introduction to the finite-difference time-domain (FDTD) method for electromagnetics,” *Synthesis Lectures on Computational Electromagnetics*, vol. 6, no. 1, pp. 1–250, 2011.
- [102] L. Inc., “Finite Difference Time Domain (FDTD) solver introduction.” [Online]. Available: <https://optics.ansys.com/hc/en-us/articles/360034914633-Finite-Difference-Time-Domain-FDTD-solver-introduction> (Accessed Aug. 2022).
- [103] J. Park *et al.*, “Performance improvement in silicon arrayed waveguide grating by suppression of scattering near the boundary of a star coupler,” *Appl. Opt.*, vol. 54, no. 17, pp. 5597–5602, Jun. 2015, doi: [10.1364/AO.54.005597](https://doi.org/10.1364/AO.54.005597).
- [104] S. Kim and M. Qi, “Post-fabrication trimming on silicon nitride photonic Bragg grating add-drop filter,” in *Frontiers in Optics 2014*, ser. OSA Technical Digest (online). Optical Society of America, Oct. 2014, Conference Proceedings, p. FTu4D.5, doi: [10.1364/FIO.2014.FTu4D.5](https://doi.org/10.1364/FIO.2014.FTu4D.5).
- [105] Z. Zhan *et al.*, “Adaptive Particle Swarm Optimization,” *IEEE Trans. Syst., Man, Cybern. C*, vol. 39, no. 6, pp. 1362–1381, Dec. 2009, doi: [10.1109/TSMCB.2009.2015956](https://doi.org/10.1109/TSMCB.2009.2015956).
- [106] S. Pathak *et al.*, “Comparison of AWGs and Echelle Gratings for Wavelength Division Multiplexing on Silicon-on-Insulator,” *IEEE Photon. J.*, vol. 6, no. 5, pp. 1–9, Oct. 2014, doi: [10.1109/JPHOT.2014.2361658](https://doi.org/10.1109/JPHOT.2014.2361658).



Appendix A — Phase correction for RSoft simulation model

A.1 Phase correction

Given that the BPM provided by RSoft is utilized with non-rotatable field monitor, a phase-correction step should be involved between two FPRs simulations. The default executable program “phasecor.exe” offered by RSoft was replaced with a user-defined python function, considering the wider mode was employed in the AWG to reduce the side-wall roughness. Detailed contents of the python file as well as the mastering callers are provided at [the Github repository](#).



Appendix B — Adaptive particle swarm algorithm (APSO)

B.1 Introduction

To find the extremum of a figure of merit function more efficiently, an user-defined Lumerical functional script was employed during the optimization of the broadband asymmetric directional coupler with the aim of dropping signal. To meet the Lumerical optimization configuration, three separate scripts named “APSO_first.lsf”, “APSO_next.lsf”, and “UDA_fom” were developed for “first generation”, “next generation”, and “fom function” of the optimization. The adaptive parameters of APSO in terms of generation are depicted in the following page. One can find the related files at [the Github repository](#).

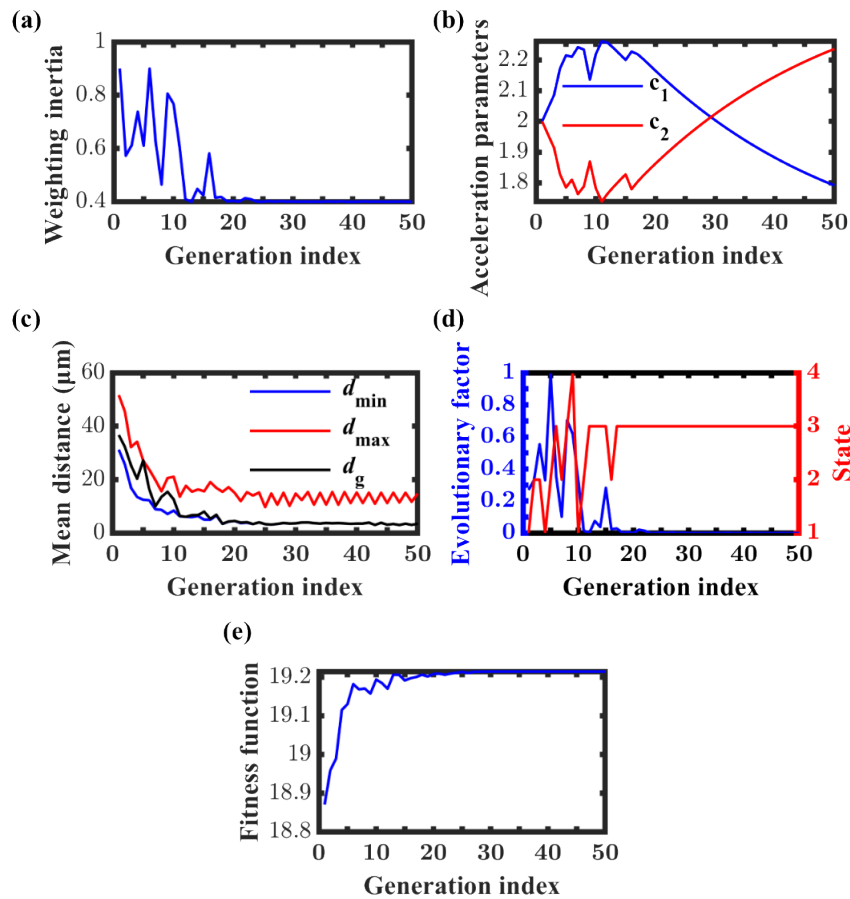


Figure B.1: (a) Weighting inertia, (b) acceleration parameters, (c) mean distance in micron, (d) evolutionary factor and its corresponding fuzzy state, and (e) fitness function.



Appendix C — Automated python process flow for Lumerical optimization on Taiwania 3 handled by local PC

C.1 Introduction

To efficiently perform optimizations under Lumerical over the cloud cluster supercomputer provided by Taiwan government, a user-defined python script allowing for automated actions including logging in, uploading, submitting, monitoring, and downloading jobs was utilized. One can find the user-defined python sscript at [the Github repository](#).